Applied Thermal Engineering 271 (2025) 126288



Contents lists available at ScienceDirect

Applied Thermal Engineering

journal homepage: www.elsevier.com/locate/apthermeng



Research Paper

Numerical and experimental investigation on extreme optimization of thermal behavior for large-capacity battery modules with rear-inlet air cooling

Yansen Zhang [a], Weikuo Zhang [b,*], Xiaoping Tang [b], Wenjun Kong [a,c,*]

[a] School of Astronautics, Beihang University, Beijing 102206, China
[b] Huadian Electric Power Research Institute Co., Ltd., Hangzhou 310030, China
[c] National Key Laboratory of Aerospace Liquid Propulsion, Beihang University, Beijing 102206, China

ARTICLE INFO

Keywords:
Large capacity
Rear air-cooled battery module
Temperature characteristics
Channel structure
Extreme cooling performance

ABSTRACT

The performance and lifetime of batteries are significantly affected by temperature. Therefore, a novel airflow channel with synergistic cooling enhancement is proposed for typical rear-inlet air-cooled lithium iron phosphate (LFP) energy storage battery modules to explore the cooling mechanisms. Initially, considering the feasibility of structural adjustment, a novel rectification structure is proposed. Both simulations and experiments yield considerable improvements, demonstrating the rationality of optimization. Subsequently, two novel structures are proposed: harmonica pipe and heat exchange fin plate. Simulation studies show that among the three novel structures, the rectification structure can achieve the greatest improvement under any circumstances. The harmonica pipe and heat exchange fin plate structure exhibit their inherent superior heat exchange capabilities only when the rectification structure is present, revealing the enabling synergistic amplification effect of rectification structure on auxiliary structures. In addition, the optimal balance between the heat exchange area of the harmonica pipe and the wind speed is achieved, thereby maximizing the overall cooling effect. After extreme optimization, the cooling efficiency increases to 0.61 (64.9 %), and the maximum temperature rise decreases by 8.6 °C (36.9 %). Both temperature differences are less than 1 °C, with respective decreases of 5.4 °C (88.5 %) and 1.3 °C (56.5 %). The optimized flow channel achieves near extreme cooling efficiency and performance. Meanwhile, the cooling performance of final optimization is significantly improved under different ambient temperatures and charging rates, demonstrating its excellent universal applicability. The results of this study provide substantial and effective guidance not only for the rear air inlet method but also for other airflow methods and other domains such as the thermal management design of power batteries.

1. Introduction

In the field of modern energy, renewable energy sources such as solar and wind power develop rapidly. However, their inherent volatility and intermittency make the generated electrical energy unsuitable for direct use [1]. Electrochemical energy storage technology effectively addresses this issue. This technology can continuously store unstable and intermittently generated electricity, providing stable and directly available power output [2,3]. The operational capability of electrochemical energy storage systems to discharge during peak demand or power supply shortages, particularly in grid frequency regulation and peak shaving applications, demonstrates critical load-balancing functionality for maintaining grid stability. This inherent advantage directly correlates with surging global adoption rates of these technologies across national energy infrastructures. Lithium-ion batteries are the preferred storage medium, with advantages such as high energy density, good cycling stability, and long lifespan. However, they have strict temperature requirements [4,5]. During battery operation, heat is generated. In the absence of timely heat dissipation, there may be a risk of overheating [6]. The safe operating temperature range of batteries is typically between 20 °C and 40 °C. Excessive temperatures can disrupt the stability of internal chemical reactions, reduce battery performance and lifespan, and even cause thermal runaway accidents [7,8]. In addition, large temperature differences within the energy storage system can lead to inconsistent battery performance and reduce overall efficiency. Therefore, ensuring the stability, safety, and operational efficiency of energy storage systems necessitates the implementation of an advanced battery

* Corresponding authors at: School of Astronautics, Beihang University, Beijing 102206, China (W. Kong).
E-mail addresses: weikuo-zhang@chder.com (W. Zhang), wjkong@buaa.edu.cn (W. Kong).

https://doi.org/10.1016/j.applthermaleng.2025.126288
Received 23 December 2024; Received in revised form 28 February 2025; Accepted 19 March 2025
Available online 22 March 2025
1359-4311/© 2025 Elsevier Ltd. All rights are reserved, including those for text and data mining, AI training, and similar technologies.

Nomenclature

$c_{p,a}$	specific heat of air,($\mathbf{J kg^{-1} K^{-1}}$)
$c_{p,b}$	special heat of battery,($J\,kg^{-1}\,K^{-1}$)
$C_{1\varepsilon}$	empirical parameter
$C_{2\varepsilon}$	empirical parameter
C_{μ}	empirical parameter
G_b	turbulent kinetic energy caused by buoyancy effects
G_k	turbulent kinetic energy generation result of meanvelocity
h	convective heat transfer coefficient,($W\,m^{-2}\,K^{-1}$)
k_a	turbulent kinetic energy
L	total thickness of battery,(m)
m	number of harmonica pipe rib
P	pressure of air, (Pa)
Q	average heat generation rate per unit volume,($W\,m^{-3}$)
q	average heat generation rate,(W)
Re	Reynolds number
S_k	source terms of k
S_ε	source terms of ε
t	time,(s)
T	absolute temperature,(K)
T_a	temperature of air,(K)
$\vec{v}$	velocity of air,($m\,s^{-1}$)
w	width of harmonica pipe,(m)
Y_M	contribution of fluctuating dilatation in compressible turbulent to the total dissipation rate

Greek symbols

λ_a	thermal conductive of air,($W\,m^{-1}\,K^{-1}$)
λ_b	thermal conductivity of battery,($W\,m^{-1}\,K^{-1}$)
α_k	inverse effective Prandtl number for k
α_ε	inverse effective Prandtl number for ε
ε_a	turbulent dissipation rate
η	cooling efficiency
ρ_a	density of air,($kg\,m^{-3}$)
ρ_b	density of battery,($kg\,m^{-3}$)
μ	molecular dynamic viscosity coefficient
μ_a	dynamic viscosity of air,($kg\,m^{-1}\,s^{-1}$)
μ_t	turbulent dynamic viscosity coefficient
∇	gradient operator
ΔT	value of temperature change
ΔT_1	temperature difference between the upper surface of cells
ΔT_2	temperature difference between the aluminum busbars

Subscripts and superscripts

a	air
b	battery
max	maximum value
min	minimum value

Acronyms

BTMS	battery thermal management system
LFP	lithium–iron-phosphate

thermal management system (BTMS). Such a system must maintain optimal temperature ranges throughout battery operation while rigorously minimizing thermal gradients across the system.

Battery thermal management systems primarily employ four principal cooling methodologies: air cooling [9–22], liquid cooling [23–27], phase change material cooling [28–31], and hybrid cooling [32–38]. Air cooling demonstrates distinct advantages in structural simplicity, cost-effectiveness, deployment flexibility, and maintenance accessibility, though it's thermal regulation capacity remains constrained by inherent efficiency limitations and stringent ambient temperature requirements. Liquid cooling systems offer superior heat transfer efficiency and exceptional temperature uniformity, particularly suited for high-power applications, yet their implementation necessitates complex architectures, substantial capital investment, rigorous maintenance protocols, and containment of potential leakage risks. Phase change material cooling maintains prolonged thermal stability, proving effective in environments with significant temperature fluctuations; however, its relatively low thermal conductivity often requires integration with supplemental cooling mechanisms to ensure adequate thermal management. Hybrid cooling configurations optimize the synergistic benefits of multiple cooling technologies, achieving enhanced thermal performance and operational flexibility at the expense of increased system complexity, elevated costs, and more demanding maintenance requirements. Consequently, air cooling persists as the predominant thermal management solution in contemporary industrial energy storage applications due to its optimal balance of performance and practicality.

Numerous studies have been conducted on air cooling technology for battery modules. Compared with single-layer unidirectional flow, Na et al. [9] changed the flow pattern of cooling air to double-layer reverse flow by inserting horizontal baffles in the module. They also introduced a rectifier grid at the entrance to enhance the cooling performance of the battery modules. Lu et al. [10] found that as the size of the airflow channel increased, the maximum temperature decreased. This led to a decrease in space utilization, requiring a balance between cooling efficiency and energy density. Chen et al. [11] optimized the design of the width and angle of the inlet and outlet chambers. Liu et al. [12] observed that the optimal parameters of traditional U-shaped and Z-shaped airflow channel structures varied with changing operating conditions, and proposed a novel J-shaped airflow channel structure that adapted to different operating scenarios, thereby improving cooling performance. Regarding parallel battery modules, Chen et al. [13] and Wang et al. [14] investigated various inlet and outlet positions and found that placing them along the symmetry axis of the module produced excellent cooling effects. Li et al. [15] conducted a comprehensive evaluation of various connection topologies by adjusting parameters such as wind speed and cell spacing. It was found that the arrangement with the positive and negative terminals positioned at opposite ends, relative to the airflow direction, exhibited the best overall performance. Zhang et al. [16] studied a T-shaped airflow channel structure with one inlet and two outlets, which were aligned with the inlet by adjusting the outlet direction. They added baffles on both sides of the pipeline and optimized the pipeline size orthogonally near the central high-temperature area. The optimized pipeline structure was similar to a Y-shaped design, achieving a 90.8 % reduction in temperature difference and exhibiting strong temperature uniformity, although the improvement in cooling efficiency was minimal.

Unlike common horizontal airflow, Yu et al. [17] set the airflow direction to vertical and found that increasing the inlet area improved cooling efficiency and reduced overall temperature, while the impact of the outlet area was minimal, but the effect on temperature difference had not been explored. Hasan et al. [18] found that increasing wind speed to enhance the turbulence of cooling air between cells could improve heat transfer performance. Luo et al. [19] proposed a novel X-shaped channel structure, in which dual inlets and dual outlets were symmetrically arranged. After orthogonal analysis optimization, the maximum temperature difference was decreased by 76.5 %, demonstrating excellent performance in improving temperature distribution, while the highest temperature was reduced by 4 °. Chen et al. [20] achieved continuous transitions during battery operation between J-

shaped, U-shaped, and L-shaped channel structures by controlling the opening and closing of multiple outlet valves. Based on this, they proposed a control strategy that switched between different channel types, allowing cooling air to be directed to high-temperature zones throughout the entire process while minimizing the size of pipes near low-temperature areas, thereby reducing temperature differences. Suo et al. [21] applied four types of plenum shapes: slanted, convex, concave, and stepped, to U-shaped and Z-shaped channel structures, finding that the Z-shaped channel design with convex plenum shapes at both the inlet and outlet demonstrated the best cooling performance. Subsequently, the size and curvature of the convex plenum were designed using multi-objective optimization, resulting in a maximum temperature reduction of 35.06 % and a temperature difference reduction of 76.98 %.

The analysis reveals that current research on air-cooled energy storage battery modules predominantly emphasizes theoretical investigations, with significantly limited studies addressing industrially viable module configurations. This research gap manifests in two critical aspects: insufficient consideration of practical implementation feasibility and inadequate guidance for engineering design optimization. In response to these limitations, the present study specifically investigates typical rear air-cooled LFP energy storage battery modules, bridging the gap between theoretical exploration and industrial application. Under fixed energy consumption constraints of the energy storage system (i.e., maintaining identical fan parameters), an integrated simulation-experimental approach was established, grounded in theoretical analysis and practical application. A two-phase optimization strategy was implemented to systematically enhance cooling performance. Initially, constrained optimizations incorporating feasible module modifications were conducted through iterative simulations and experimental validation, achieving maximum performance improvements while maintaining minimal structural alterations. Subsequently, comprehensive simulation-based optimizations were performed without practical constraints to investigate structural interactions and flow channel size effects, establishing the theoretical limits of cooling efficiency. The study concluded with a dependencies analysis of ambient temperature and charging rate on thermal performance characteristics.

2. Models and methods

A thermal management mathematical model is established based on the 1P12S-280 Ah LFP battery experimental module. Simulation calculations are conducted under 1C charge rate and rear intake airflow conditions. Fig. 1 shows the rear air-cooling module and temperature measurement points. Under the pressure generated by the fan, the cooling air mainly enters from the rear inlet, with a small portion flowing in from the side. The incoming cooling air is divided into two streams: the main part passes through the longitudinal main flow channels in the center and sides, as well as above the battery cells, while the smaller part flows through the heat exchange fin plate located at the bottom of the battery. After cooling the cells, the air is collected on the front side and discharged by two fans installed on the front wall.

The temperature measurement points in this study are divided into two categories. In Fig. 1(d), the temperature measurement points are located at the center of the upper surface of each cell and are utilized to calculate the maximum temperature difference during the simulations. This is determined by subtracting the minimum value from the maximum value recorded among T1 to T12 at the end of the charging process. In Fig. 1(e), the temperature measurement points are divided into two groups: T1 to T12 are located at the center of the upper surface of each aluminum busbar, but there is no temperature measurement on the rear busbar because it is completely exposed to the cooling air; T13 to T24 are located at the center of the side surface of each cell. It should be noted that the temperature measurement points in Fig. 1(d) exist only in the simulation, while the measurement points in Fig. 1(e) exist in both the simulation and actual modules, with thermocouples installed in corresponding locations. In practical modules, the center point on the upper surface of each cell corresponds to the position of the explosion-proof valve, which is not suitable for temperature monitoring. Therefore, thermocouples are generally placed on the aluminum busbars, and the busbar temperatures are used to calculate the maximum temperature difference and maximum temperature. The experimental

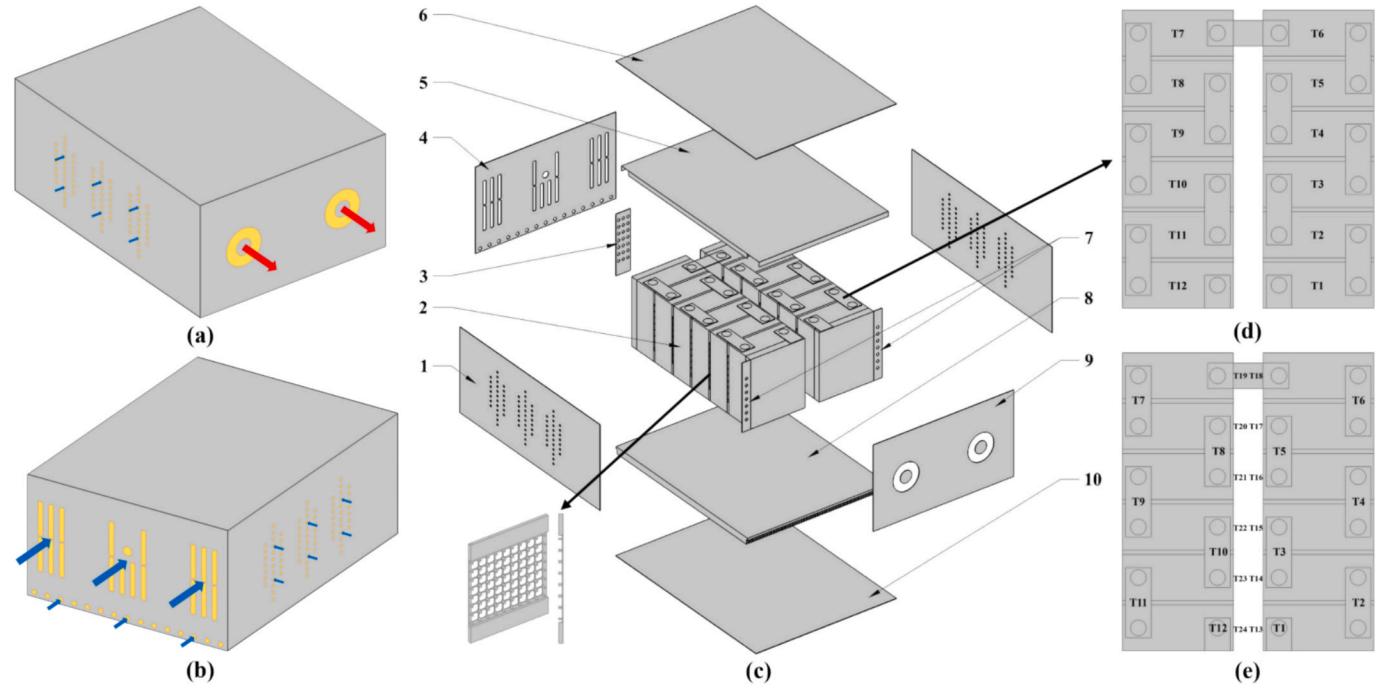


Fig. 1. The rear-inlet air-cooled module and the temperature measurement points. (a) Schematic of airflow (front); (b) Schematic of airflow (rear); (c) Detailed structure of the module (1-side wall; 2-cell section; 3-rear windshield; 4-rear wall; 5-cover plate; 6-upper wall; 7-front windshield; 8-heat exchange fin plate; 9-front wall; 10-bottom wall); (d) measurement points on upper surfaces of the cell; (e) measurement points on aluminum busbars and sidewalls of the cell.

temperatures at the measurement points in Fig. 1(e) validate the model proposed in this paper. Consequently, two temperature difference settings are defined. The first one, represented as temperature difference ΔT_1, corresponds to the measurement points located at the center of the upper surface of each cell, which is mainly used in this study. The second one is called temperature difference ΔT_2, corresponding to the measurement points located at the center of the upper surface of the aluminum busbars. At the same time, the cooling efficiency η is defined as the ratio of heat removed by the cooling air to the total heat generated by the batteries.

In this model, the battery parts were considered to be heat sources with uniform heat generation. According to the electrochemical heat generation model, the heat sources are generally divided into three parts: polarization heat, reaction heat, and ohmic heat. This model is elaborated in ref. [6]. The average heat generation rate and physical properties were measured by experiments. The thermal conductivity was measured using the hot wire method, where the K-type thermocouple was employed with a measurement error within 2.5 %. The specific heat was measured using the heating method in the accelerating rate calorimeter, where the N-type thermocouple was utilized, and the measurement error was within 1.7 %. The average heat generation rate was also measured using the accelerating rate calorimeter. In an adiabatic environment, the average heat generation rate was calculated by measuring the temperature rise during the battery charging and discharging process, with a measurement error within 2.1 %. The specific measurement methods are detailed in ref. [6]. Table 1 shows the parameters related to the LFP cell. The maximum rate of the battery is 1C, which corresponds to the highest heat generation rate. At a current of 280 A (1C rate), it was found that the heat generation rate during charging was almost the same as that during discharging. For simplicity, this study chooses the charging process as the focus of investigation.

The entire air-cooled BTMS model is divided into two parts: one involves the internal thermal conduction of the battery itself, and the other addresses the convective heat transfer between the battery and the cooling air. The Reynolds number *Re* at the fan of the air-cooled battery module is 23995, exceeding the transition *Re*, indicating that the airflow is turbulent. The turbulence model selected for this study is the *k-ε* model, with model constants set at $\alpha_k = 1.0$, $\alpha_\varepsilon = 1.3$, $C_{1\varepsilon} = 1.44$, $C_{2\varepsilon} = 1.92$ and $C_\mu = 0.09$ respectively. Table 2 presents the governing equations for the air-cooled BTMS model [6,20]. The air inlet is used as pressure inlet, while the air outlet is used as fan outlet. The gauge pressure of the fan is 143.2 Pa, and the free transfer flux is 0.035 m^3/s. The outer surface of the module is in contact with air, and the convective heat transfer coefficient is set to 4.7 $W/(m^2 \bullet K)$. The external temperature is maintained at 23.5 °C, and both the initial temperature of the model and the air inlet temperature are set to 23.5 °C. To ensure the accuracy of model validation, the boundary conditions of the model are consistent with the experimental conditions. A cross-section was established along the longitudinal direction of the module to monitor the air velocity distribution inside the harmonica pipes and the temperature distribution between the cells. The position of the monitoring surface is shown in Fig. 2. In this model, unstructured grids are utilized for meshing, and after performing grid-independence verification, the final grid count is determined to be 3.3 million. Since the verification method is identical to that in ref. [3], the detailed process is not extensively presented here.

Table 1
Relevant parameters of a LFP cell.

Parameters (unit)	Value
Capacity, (Ah)	280
Thermal conductivity λ_b, ($W\,m^{-1}\,K^{-1}$)	25.05 × 2.17 × 25.05
Specific heat $c_{p,b}$, ($J\,kg^{-1}\,K^{-1}$)	1050
Density ρ_b, ($kg\,m^{-3}$)	2146.9
Average heat generation rate q, (W)	33

Table 2
Governing equations and boundary conditions used in the air-cooled BTMS model.

Physics	Governing equations and boundary conditions	Reference
Thermal Model of Batteries		
Heat transfer equation	$\rho_b c_{p,b}\frac{\partial T}{\partial t} = \nabla(\lambda_b \nabla T) + Q\left(-\lambda_b \frac{\partial T}{\partial x}\right)_{x=L} = h(T - T_a)$	[3,6]
Flow Model of Cooling Air		
Mass conservation	$\frac{\partial \rho_a}{\partial t} + \nabla \bullet (\rho_a \vec{v}) = 0$	[14,20]
Momentum conservation	$\frac{\partial}{\partial t}(\rho_a \vec{v}) + \nabla \bullet (\rho_a \vec{v}\vec{v}) = -\nabla P + \mu_a \nabla^2 \vec{v}$	[14,20]
Energy conservation	$\frac{\partial}{\partial t}(\rho_a c_{p,a} T_a) + \nabla \bullet (\rho_a c_{p,a} \vec{v} T_a) = \nabla \bullet (\lambda_a \nabla T_a)$	[14,20]
Turbulent kinetic energy and turbulent dissipation rate	$\frac{\partial}{\partial t}(\rho_a k_a) + \frac{\partial}{\partial x_i}\left(\rho_a k_a \vec{v}_i\right) = \frac{\partial}{\partial x_j}\left(\left(\mu + \frac{\mu_t}{\alpha_k}\right)\frac{\partial k_a}{\partial x_j}\right) + G_k + G_b - \rho_a \varepsilon_a - Y_M + S_k$ $\frac{\partial}{\partial t}(\rho_a \varepsilon_a) + \frac{\partial}{\partial x_i}\left(\rho_a \varepsilon_a \vec{v}_i\right) = \frac{\partial}{\partial x_j}\left(\left(\mu + \frac{\mu_t}{\alpha_\varepsilon}\right)\frac{\partial \varepsilon_a}{\partial x_j}\right) + C_{1\varepsilon}\frac{\varepsilon_a}{k_a}(G_k + C_\mu G_b) - C_{2\varepsilon}\rho_a \frac{{\varepsilon_a}^2}{k_a} + S_\varepsilon \mu_t = \rho_a C_\mu \frac{{k_a}^2}{\varepsilon_a}$	[14,20]

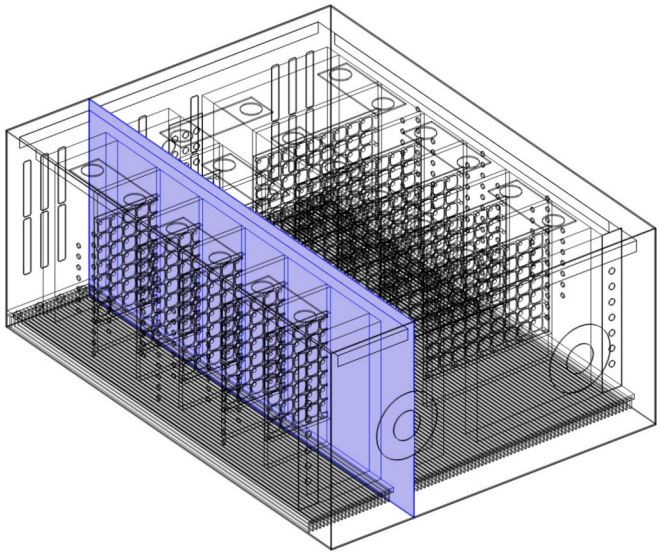


Fig. 2. The position of the monitoring surface.

3. Experimental

3.1. Experimental setup

Fig. 3 shows the experimental system, which consists of a control system, a power conversion system, a battery module, a temperature acquisition device, and a thermal imaging instrument. During the experiment, the control system first sends charging and discharging commands to the power conversion system, which then executes these commands on the battery module. Throughout the process, the temperature acquisition device records the temperatures of each measurement point on the battery module at a frequency of once per second. Upon completion of the experiment, the fan is immediately turned off, the module cover is immediately opened, and the temperature distribution data of the battery is collected using the thermal imaging instrument. If this step is not performed promptly, the high-temperature

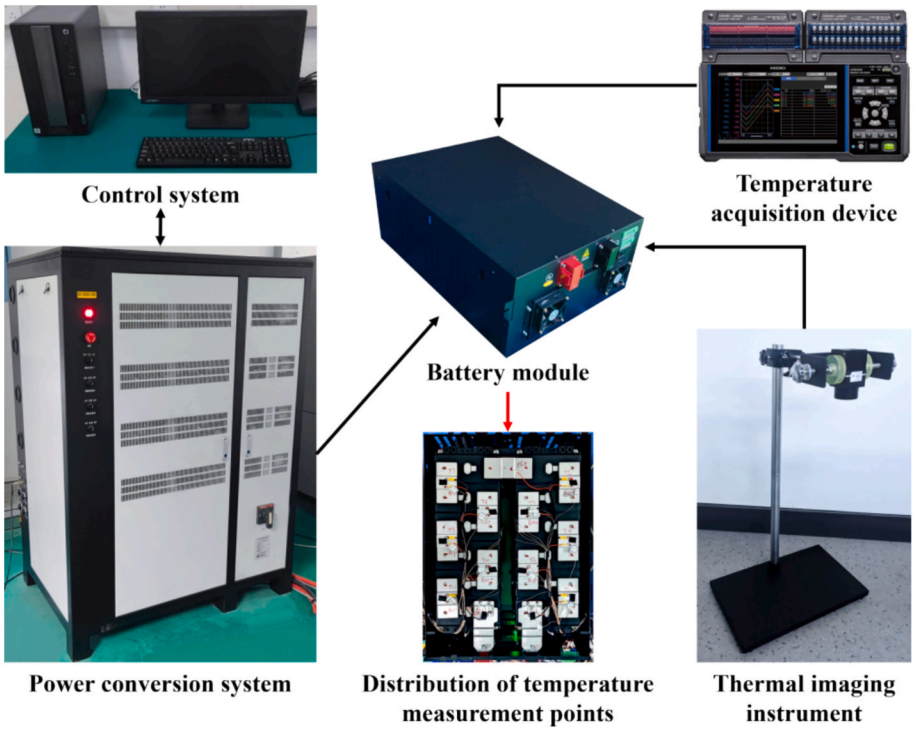


Fig. 3. The experimental system.

cells may rapidly cool upon contact with lower-temperature ambient air, resulting in the temperature data of the thermal imaging instrument being lower than the temperatures at the end of the experiment.

3.2. Charging and discharging steps

This experiment comprises two complete charge and discharge cycles of the battery module. After the initial charging and discharging phase, an additional cycle is performed with a 10-minute break between each step, during which the fan remains running continuously. The sequence is: charge-rest-discharge-rest-charge-rest-discharge. The specific steps are as follows:

(1) The battery module has been fully discharged, ensuring that the temperatures at all measurement points remain stable and unchanged.
(2) The module is charged with a constant current of 1C until the maximum voltage of each individual cell reaches 3.65 V, at which point the charging is terminated. A 10-minute break follows. The module then discharges at 1C until the minimum voltage of each individual cell drops to 2.5 V, concluding the discharge process. This completes the initialization phase, followed by taking another 10-minute break.
(3) Charge the module again with a constant current of 1C until the maximum voltage of each individual cell reaches 3.65 V, and then terminate the charging. A 10-minute break is taken afterward.

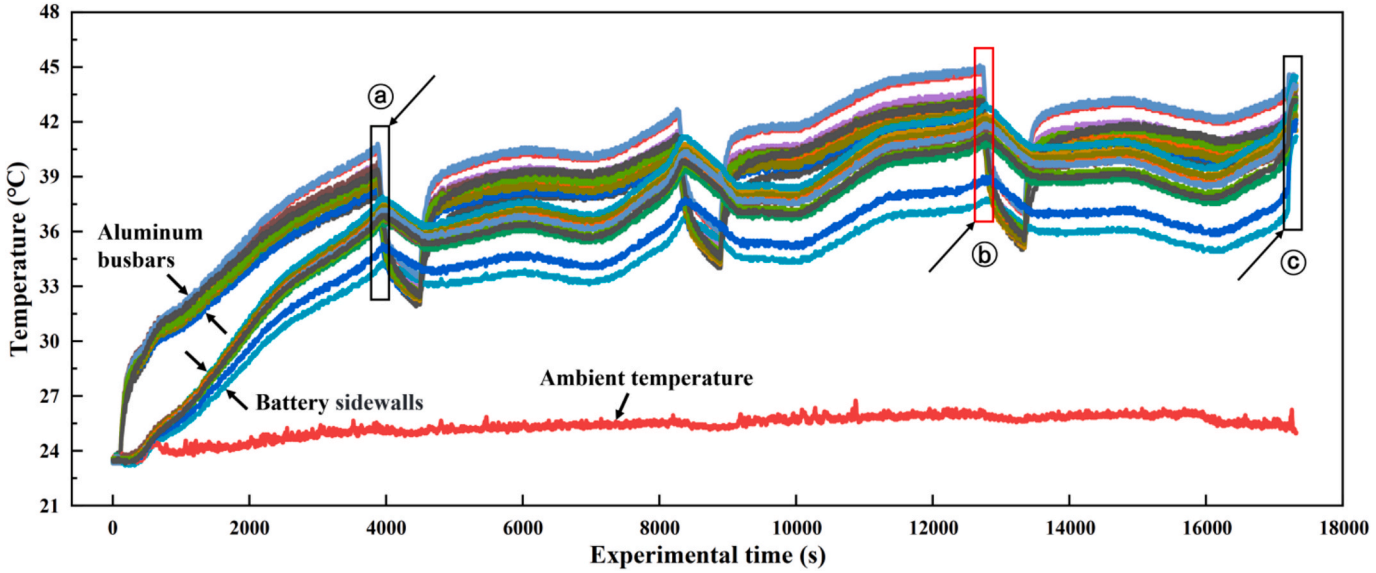


Fig. 4. Temperature trends at each measurement point during the experiment.

Subsequently, the module discharges at 1C until the minimum voltage of each individual cell drops to 2.5 V, and the discharge process ends. Therefore, the entire charge and discharge experiments are completed.

4. Results and discussion

4.1. Experimental results

Fig. 4 presents the temperature variation trends at different measurement points in the experiment. The experiments were conducted in a temperature-controlled laboratory, where the variation curve of the ambient temperature is shown by the red line in Fig. 4. The initial temperature was 23.5 °C. Although the ambient temperature increased slightly during the experiment, the magnitude of this increase was negligible, and its impact on the battery temperature could be disregarded. As the experiment progressed, the cell temperature gradually increased, and it decreased during the rest periods. As shown in Fig. 4, the curves representing higher temperatures corresponded to the aluminum busbars, while the curves representing lower temperatures were the measurement points on the cell sidewall. The temperature at the end of the first charging cycle was marked as point ⓐ, which was used to validate the numerical model in the simulation. Since the maximum temperature was recorded at the end of the second charging cycle, as shown in point ⓑ, this temperature was chosen to compare the cooling effect before and after optimizing the module flow channel structure. The temperature at the end of the last discharge (marked as point ⓒ) was compared with the temperature data collected by the thermal imaging instrument for verification. Due to the limitation of not being able to open the module during the experiment, the thermal imaging instrument could only capture the temperature at the end of the experiment. It was worth noting that during the rest period, the temperature drop rate of the aluminum busbar was higher than that of the cell sidewalls. For example, at point ⓐ, the temperatures of the aluminum busbars were higher than those of the sidewalls at the end of charging, but after the rest period, the temperatures of the aluminum busbars dropped to be lower than those of the sidewall temperatures. When charged again, the temperatures of the aluminum busbars rapidly increased, exceeding the sidewall temperatures in a short period of time. This behavior could be analyzed as follows: the heating in aluminum busbars was mainly caused by Ohmic heating, which was proportional to the square of the current. Considering that the current in this experiment was 280 A, which was relatively high, the heating rate of the aluminum busbars was also correspondingly high. In addition, the specific heat of the aluminum busbars was slightly lower than that of the cells body, leading to a more sensitive temperature change of the aluminum busbars than the cell sidewalls.

Fig. 5 shows the layout of measurement points and the temperature distribution at different time points. It was evident that the overall temperature distribution exhibited good symmetry, with the temperatures of the aluminum busbars consistently higher than those of the sidewalls. The high temperatures on the aluminum busbars were observed at points T3 and T10, while lower temperatures were recorded at points T1, T2, T6, T7, T11, and T12, indicating that the high-temperature region was moving forward. In addition, the temperatures at the rear and outside of the aluminum busbars were still relatively low. This phenomenon could be attributed to the forward flow of cooling air, which resulted in a lower air temperature at the rear busbar. Points T1, T2, T11, and T12, located in the front and outside, effectively came into contact with the cooling air, while points T3 and T10, located closer to the center and front, had less airflow and higher air temperatures. High temperatures were observed on the sidewall at points T14 and T24, while low temperatures were found at points T18 and T19. The overall temperature at the front side of the module was higher than that at the rear side, and the temperature generally increased from rear to front. This trend was also a result of the forward flow of cooling air.

Fig. 6 shows the thermal imaging temperature distribution of the module at the end of the experiment, as well as a comparison with the experimental temperature data. The temperature distribution clearly indicated that the high-temperature region was moving forward, with the maximum temperature located at the point indicated by the black arrow. It was worth noting that no such peak temperature was observed on the aluminum busbars. On the contrary, it was located on the upper surface of the cell near the aluminum busbar of row ②. Two analyses explained this observation. Firstly, during the interval between the end of the experiment and the start of thermal imaging, the temperatures of the aluminum busbars decreased slightly. As shown in Fig. 4, the temperatures of the busbars rapidly decreased during the rest period, indicating a high temperature sensitivity. Furthermore, the estimated time delay when turning off the fan and turning on the module was about 15 s, resulting in a slight decrease in temperature. Secondly, as shown in Fig. 5, the highest temperature of the sidewall was close to that of the aluminum busbars. Given that the cooling conditions at the measurement points on the sidewall were superior to those on the upper surface of the cells, it was expected that the temperature on the upper surfaces of the cells would exceed that on the sidewall. These two reasons together

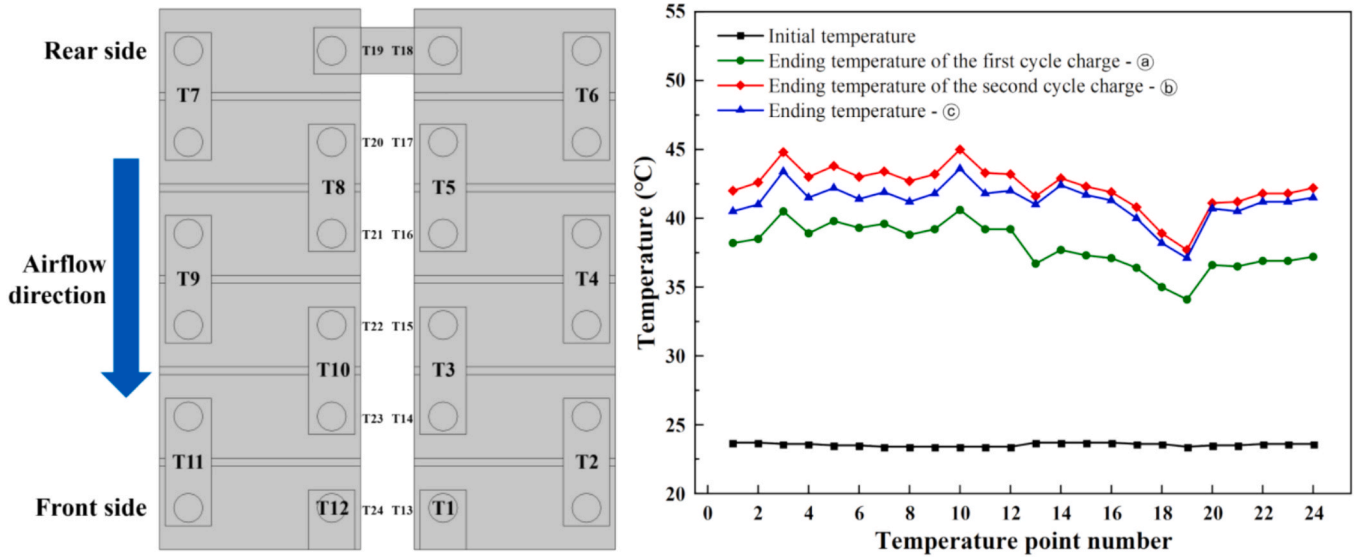


Fig. 5. The layout of measurement points and temperature distribution at different time points.

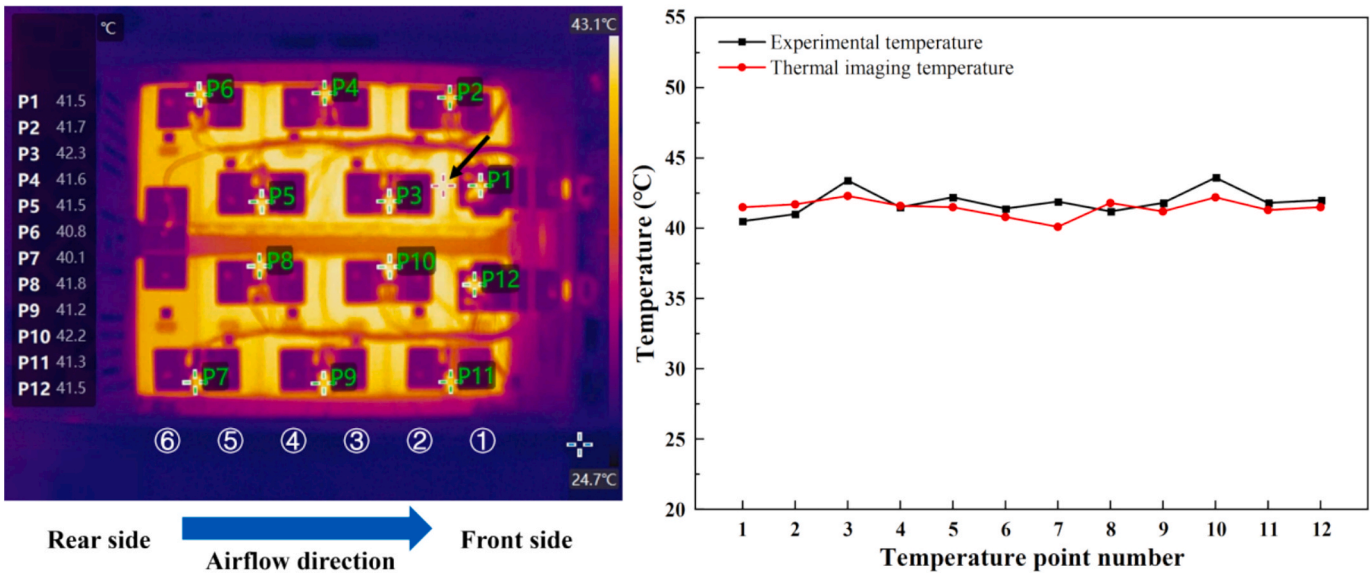


Fig. 6. Thermal imaging temperature distribution and its comparison with experimental temperature.

explained the observation that the highest temperature was not on the aluminum busbars. Comparison showed that the maximum error was 1.8 °C and the root mean square error was 0.9 °C, indicating good overall agreement. Although the temperatures of the aluminum busbars had slightly decreased, the magnitude of the decrease was very small. Therefore, it could be inferred that the maximum temperature on the upper surface of the cells was sometimes almost equal to or even slightly higher than the maximum temperature of the aluminum busbars. The strong correlation in temperature measurement further validated the accuracy of the thermal imaging data obtained in this experiment.

4.2. Model validation

Under the condition that the initial temperature and cell parameters are consistent, the comparison between the temperature calculated by numerical simulation and the experimental temperature at the end of the first charging cycle is shown in Fig. 7. The specific locations of the thermocouples corresponding to the measurement point numbers are shown in Fig. 1(e). The maximum error was recorded at 1.4 °C, while the root mean square error was 0.77 °C. The highest temperature measured was 40.6 °C, with a maximum error of 3.4 % and a root mean square error of 1.9 %. These relatively small error percentages indicated good fitting and demonstrated the accuracy of the numerical model calculations.

4.3. Simulation results

The simulation calculations of the module were conducted at a charging rate of 1C. The trends of the maximum, average, and minimum surface temperatures of the battery at an initial temperature of 23.5 °C, as well as the temperature differences between the cells during charging, are shown in Fig. 8. As charging progressed, the overall temperature increased and the temperature differences between the cells gradually widened. At the end of the charging process, the maximum, average, and minimum surface temperatures of the battery were recorded as 46.8 °C, 38.6 °C, and 29.7 °C, respectively, with the $\Delta T_1 = 6.1$ °C and the $\Delta T_2 = 2.3$ °C. After calculation, the η was 0.37. The maximum temperature exceeded 40 °C, and the elevated ΔT_1 was also significant, which did not meet safety requirements. The η was also at a lower level. Therefore, optimization of the flow channel structure was essential.

The temperature distribution changes on the surfaces of the cells during the charging process are shown in Fig. 9. As the charging

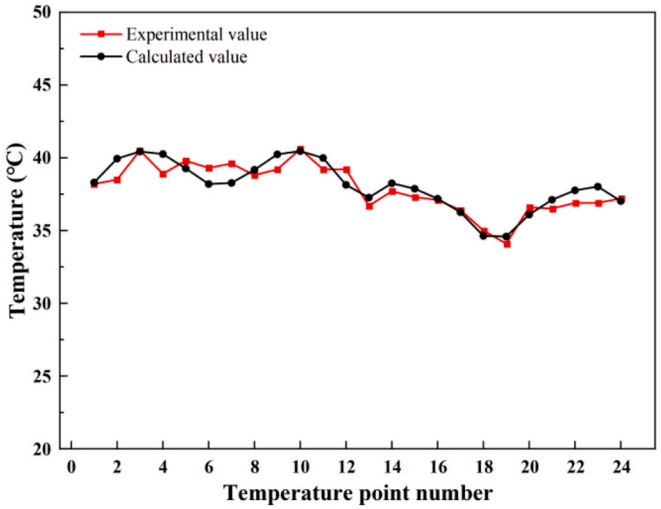


Fig. 7. Comparison of calculated and experimental temperatures.

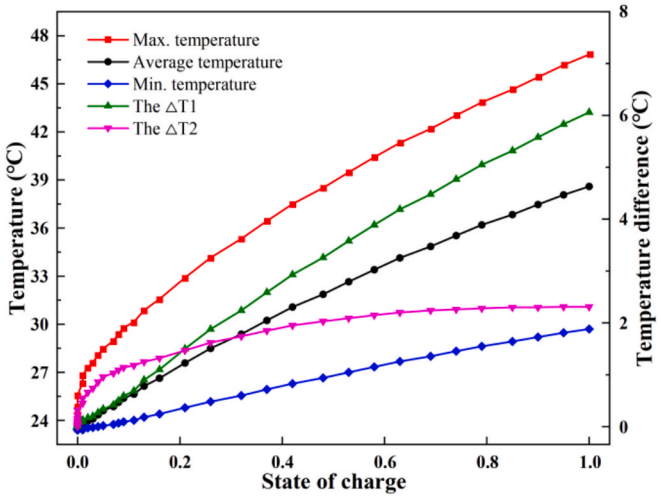


Fig. 8. Calculated temperature trends during charging.

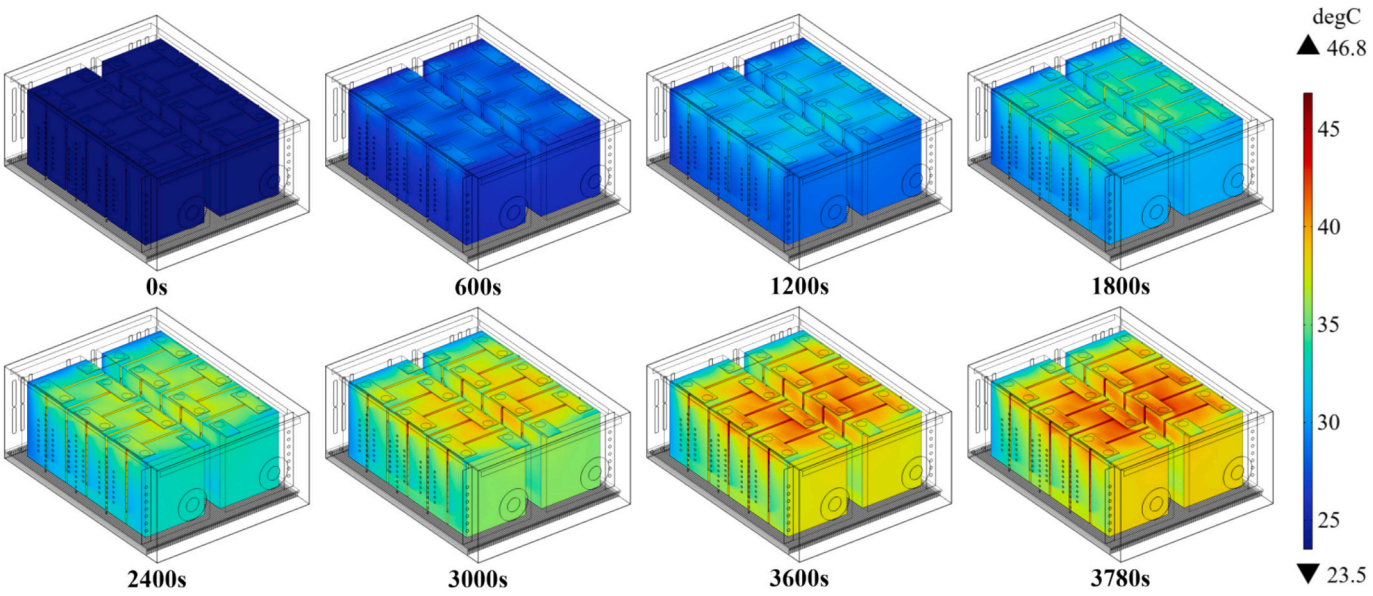


Fig. 9. The temperature distribution changes during charging.

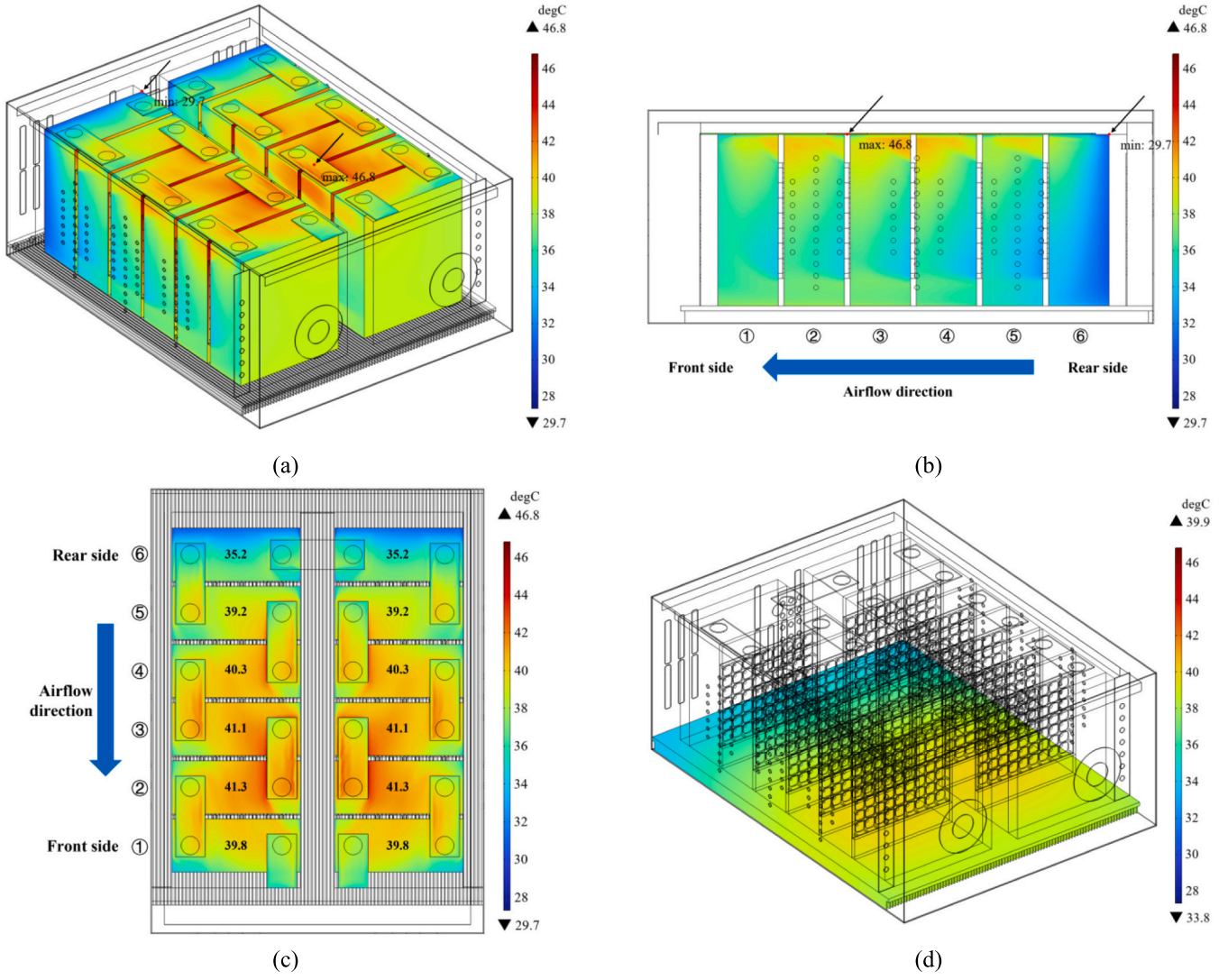


Fig. 10. Upon the completion of charging, the temperature distribution of cells and heat exchange fin plate.

progressed, the overall temperature of the cells increased, and the temperatures of the aluminum busbars and their surrounding areas were higher compared to other regions of the cells. This could be attributed to two main reasons. Firstly, the heat in the aluminum busbars mainly resulted from Ohmic heating, which was strictly proportional to the square of the current. In contrast, the heat generation inside the cells not only included Ohmic heating, but also reaction heat and polarization heat, among which reaction heat and Ohmic heating were the main components. The magnitude of the heat of reaction depended on the thermodynamic characteristics of the internal chemical reactions and was influenced by the charging and discharging states, current, and battery temperature, where the reaction heat was approximately linearly proportional to the current. Assuming a charging rate of 1C in this case, compared to a charging rate of 0.5C, the increase in heat generation rate in the aluminum busbars is greater than that of the cells. Secondly, since the material of the aluminum busbars is aluminum with a specific heat of 900 J/(kg·K), while the specific heat of the cell body is 1050 J/(kg·K), the specific heat of the aluminum busbars is slightly lower than that of the cell body. Consequently, the temperature rise in and around the aluminum busbars was higher.

Upon completion of charging, the temperature distribution of the cells and heat exchange fin plate is shown in Fig. 10. Fig. 10(a) and (b) indicated that the highest temperature occurred at the interface between the aluminum busbars and the harmonica pipes, while the lowest temperature occurred on the rear wall of row ⑥. In actual temperature measurements of the module, the detected temperature points were all located on the outer surfaces of the cells, and the temperatures at the interface with the harmonica pipes could not be measured. However, as shown in Fig. 10(a), the temperatures in the high-temperature regions of these contact interfaces exceeded the actual measured outer surface temperatures. Consequently, during the operation of the module, the high-temperature regions were not located on the aluminum busbars; rather, they were located on the surfaces in contact with the harmonica pipes. Despite their high heat generation rate, the aluminum busbars were effectively cooled by direct contact with air. In contrast, the contact surfaces between the cells and the harmonica pipes, lacking direct airflow for cooling, relied on the harmonica pipes for heat dissipation. Therefore, the temperatures in the high-temperature regions of these contact surfaces might exceed those of the aluminum busbars. It should also be noted that these high-temperature areas on the contact surfaces were generally located near the aluminum busbars, and the overall temperature of the contact surface increased as it approached the front.

In contrast to the temperature distribution of the cells in the side air intake configuration, the high-temperature regions of the module in the rear-inlet air-cooled configuration were closer to the front, exhibiting an asymmetrical temperature distribution along the vertical axis. In the side air intake module, the high-temperature regions were centered, and the temperature distribution was approximately front-rear symmetrical [3]. As shown in Fig. 10(c), the highest temperature was found in row ② of cells, while the lowest temperature was observed in row ⑥ of cells. The temperature of row ⑥ of cells was significantly lower than that of the first five rows, being 4 °C lower than the adjacent row ⑤ of the cells, and the ΔT_1 was 6.1 °C. After excluding the row ⑥ of the cells, the ΔT_1 was reduced to 2.1 °C. The notably low temperature of row ⑥ of the cells was primarily due to the flow of cooling air moving from rear to front. The row ⑥ of the cells first encountered the cooling air, at which point the temperature was the lowest, thereby maximizing heat exchange efficiency and resulting in lower temperatures of the row ⑥ of cells. Additionally, the direction of the bottom heat exchange fin plate also followed vertical alignment, leading to a temperature distribution trend with higher temperatures in the front and lower temperatures at the rear. The temperature of the fin plate beneath row ⑥ of cells was lower than that of the fin plate below the first five rows of cells. The portion of the finned plate in contact with the first five rows exhibited a more uniform and higher temperature distribution, further exacerbating the longitudinal temperature difference within the module, ultimately causing the temperature of row ⑥ of cells to be significantly lower than that of the first five rows.

At the end of charging, the velocity field of the air is shown in Fig. 11. As shown in Fig. 11(a), the cooling air mainly entered through the inlet on the rear wall. Although there were air intakes on the side walls, the airflow was minimal. Therefore, this paper still defined the intake mode of the module as rear-inlet. The incoming cooling air mainly flowed through three longitudinal main channels, as well as channels above the cells and the heat exchange fin plate. It ultimately converged at the front and was expelled by the fan. As shown in the cross-sectional velocity data in Fig. 11(b), the airflow velocity inside the red-framed harmonica pipes was the lowest, even lower than that inside the heat exchange fin plate. This indicated that the amount of cooling air passing through the harmonica pipes was minimal, leading to insufficient heat exchange performance. This could be mainly attributed to the fact that although two types of windshields (3-rear windshield and 7-front windshield in Fig. 1) were added to the module in an attempt to direct cooling air to the harmonica pipes, these windshields contained numerous ventilation holes. Moreover, there was a relatively large channel between the cells and the cover plate, which ultimately hindered these windshields from effectively guiding the cooling air to the harmonica pipes.

The cross-sectional temperature distribution in Fig. 12 clearly illustrates the characteristic temperature distribution of the rear-inlet module, where the high-temperature zone moved forward. However, the highest temperature was not in the row ① of cells, but in the row ②. This was mainly due to the phenomenon of mutual heating between cells. The row ① of cells was only adjacent to one side and exposed to cooling air on the other side, whereas the row ② of cells was surrounded by other cells on both sides, leading to mutual heating and thus a higher overall temperature. The black-framed region highlighted the relatively high air temperature inside the harmonica pipes, primarily due to the airflow velocity inside the harmonica pipes being insufficient to effectively remove the heat. The temperature distribution of the air in the bottom heat exchange fin plate was higher in the front and lower in the rear. Although the airflow velocity inside the heat exchange fin plate was higher than that inside the harmonica pipes, the longer flow path resulted in the air temperature at the end of the path ultimately being higher than that inside the harmonica pipes.

4.4. Preliminary optimization study

4.4.1. Simulation optimization

It was evident from the analysis in Section 4.3 that the current channel structure of the module did not effectively utilize the cooling air. The highest temperature region of the entire module was located at the contact surfaces between the cells and the harmonica pipes, where the minimum amount of cooling air passed through the harmonica pipes. Most of the cooling air passed through the longitudinal main channels without timely contact and heat exchange with the cell surfaces, resulting in poor cooling efficiency. Based on this, the preliminary optimization of this study focused on adjusting the cover plate, rear baffle, and windshields to effectively guide the cooling air through the harmonica pipes and heat exchange fin plate, thereby enhancing cooling efficiency. These optimizations were also practical, making it easy to make corresponding adjustments in actual modules. The specific structural improvements are shown in Fig. 13. Optimizing I-1 involved modifying the cover plate by extending it so that the front wall of the cover plate contacted the front wall of the module, and the rear wall of the cover plate also contacted the rear wall of the module. In addition, the sides of the cover plate were also filled. Optimizing I-2 involved adding a rear baffle at the back of the cells, blocking the air inlet of the channel between the cells and the cover plate, thereby reducing the amount of cooling air in that channel. This reduced the direct cooling effect on the upper surface of the last row of cells, aiming to increase the temperature at the monitoring points of the last row of cells and reduce the temperature difference. It also increased the wind resistance at this

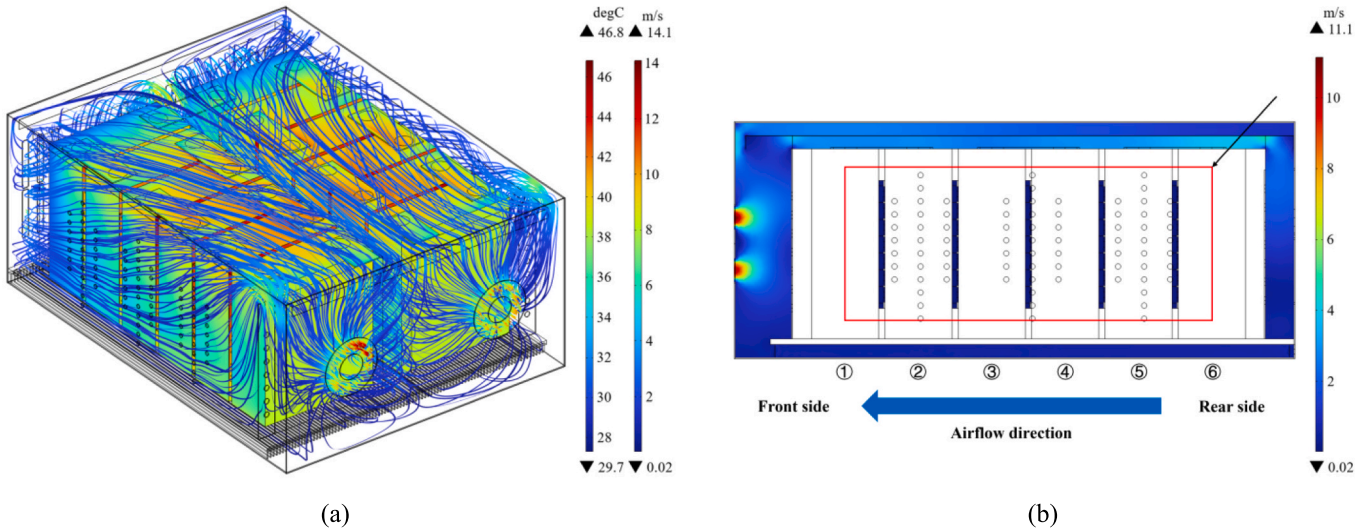


Fig. 11. At the end of charging, the velocity field of the air.

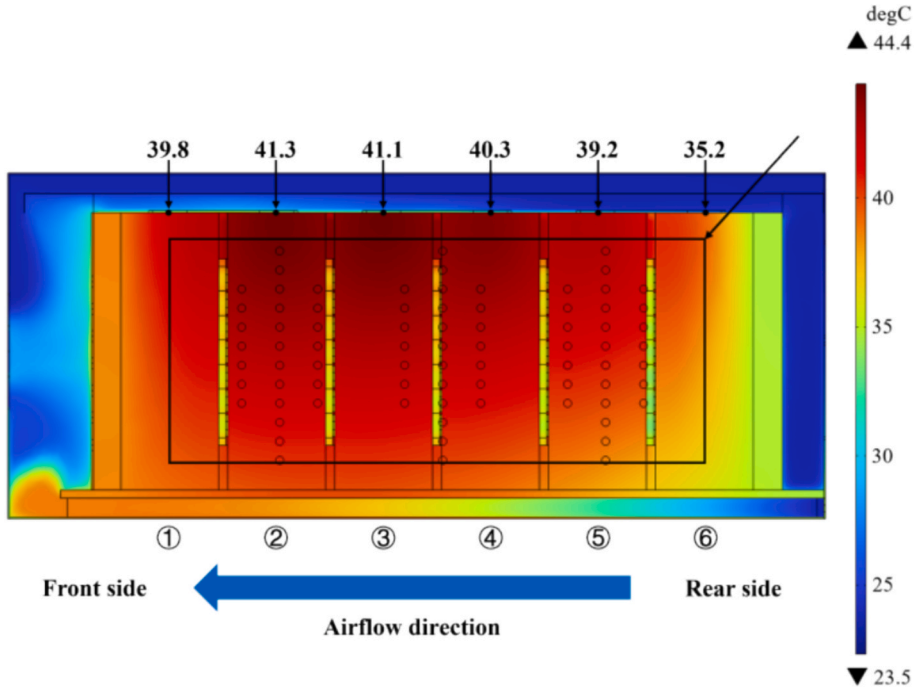


Fig. 12. At the end of charging, the cross-sectional temperature distribution.

location, guiding the cooling air smoothly to the harmonica pipes. Optimizing I-3 involved modifying the windshields, specifically removing all ventilation holes and adding a horizontal windshield above the front windshield. The horizontal windshield could contact the front end of the improved side of the cover plate, jointly adjusting the flow channel at the front end of the module to ensure that all cooling air reached the fan only through the harmonica pipes and heat exchange fin plate.

The preliminary improvement effect of the channel structure is shown in Fig. 14(a). It was evident that the overall temperature and temperature difference of the cells had been improved in the optimized structure. The maximum temperature rise on the cell surfaces reduced by 2.7 °C, the average temperature rise reduced by 4.5 °C, and the minimum temperature rise reduced by 2.3 °C. The maximum temperature rise of the aluminum busbars had reduced by 2 °C, and the ΔT_1 had reduced by 1.2 °C. The η had increased to 0.54 (45.9 %). It was worth noting that significant improvements were observed in the average temperature rise and efficiency η, which represented the overall cooling efficiency of the channel structure. This indicated that the preliminary optimization was effective. Considering the feasibility of structural modifications in the actual modules, the degree of structural adjustments was relatively small. However, there was still significant improvement in cooling performance.

Fig. 14(b) shows that after preliminary optimization, the actual airflow path has undergone significant changes. Upon entering the module, the cooling air was divided into two streams. Most of them first flowed into the lateral longitudinal main channels, passed through the harmonica pipes, then into the central longitudinal main channel, and ultimately reached the vicinity of the fan. A small portion of the airflow remained unchanged and continued to flow longitudinally along the

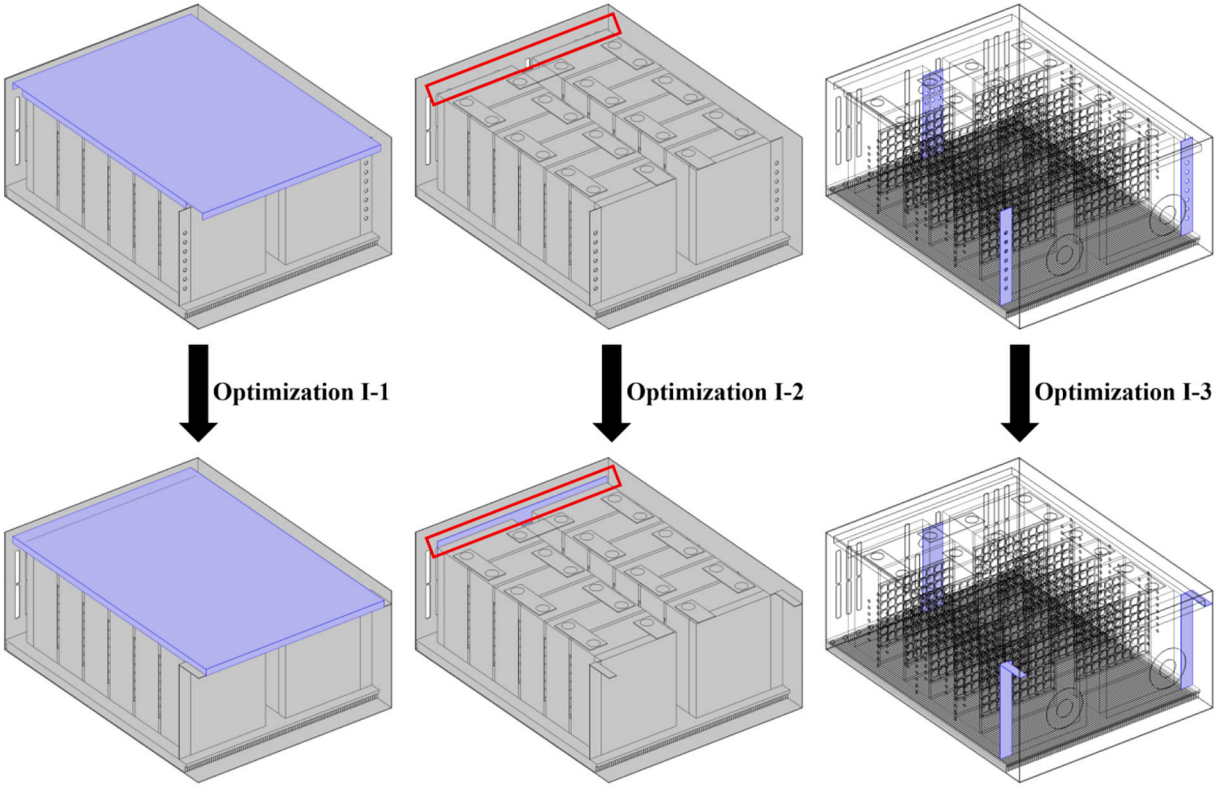


Fig. 13. Three structural improvements in preliminary optimization.

heat exchange fin plate towards the fan area, where the two airflows converged before being expelled by the fan. The designated airflow path had been established. However, due to the limited cross-sectional area of the lateral longitudinal main channels, the air flowing towards the forefront of the harmonica pipes would encounter considerable flow resistance. Therefore, it turned upward, flowed through the channel between the cover plate and the upper wall of the module, bypassed the central harmonica pipes, and then entered the forefront harmonica pipes. This phenomenon slightly disrupted the predefined airflow path and exacerbated the chaos within the flow field.

Fig. 14(c) and (d) indicated that after preliminary optimization, the airflow velocity in the harmonica pipes and the heat exchange fin plate significantly increased, corresponding to a significant decrease in air temperature. This effectively enhanced the utilization rates of the cooling air. In the initial optimization plan, the aim was to increase the temperature of the row ⑥ of cells to reduce the ΔT_1; however, this approach did not produce the expected results. The analysis showed that although a rear-baffle was added to the rear side of the cells to minimize direct cooling of the row ⑥ of cells by the cooling air, the airflow velocity in the heat exchange fin plate and the final harmonica pipes significantly increased. Consequently, the cooling effect on the row ⑥ of cells had been improved, leading to a decrease in the temperature of the row ⑥ of cells, which was originally intended to increase. Moreover, the temperature drop at the highest point was more pronounced, resulting in an overall reduction in the ΔT_1.

4.4.2. Experimental optimization

In order to verify the improvement effect of optimization I-1, 2, and 3 described in section 4.4.1, corresponding modifications were made to the actual module structure, as shown in Fig. 15. Fig. 13 and its accompanying explanations provided a detailed description of these improvements; thus, they would not be repeated here. After the second charging cycle, Fig. 16 shows the experimental results comparing the effects before and after optimizations I-1, 2, and 3. All measurement points showed varying degrees of temperature reduction, with the average temperature of the aluminum busbars demonstrating the most significant improvement, decreasing by 6.2 °C (31.3 %). The average temperature of the sidewall also improved by 3.9 °C (22.0 %), confirming that the overall cooling efficiency of the modified channel structure had indeed been enhanced. The optimization strategy for temperature differences involved reducing the temperature in high-temperature areas and increasing the temperature in low-temperature areas. The temperature difference between the side walls decreased by 1.8 °C (34.6 %). Furthermore, the temperature distribution along the side walls indicated that, although the overall temperature decreased, the reduction in the high-temperature areas was greater than that in low-temperature areas. This resulted in an improvement in temperature distribution, further validating the rationality of this optimization approach and corresponding structural modifications. The optimized structure obtained from the simulation results had been effectively applied to the design of the actual modules, significantly improving the cooling performance. This strongly demonstrated the effectiveness and practicality of the research conducted during the simulation phase in guiding the optimization of the actual module's channel structures.

4.5. Extreme optimization study

Given that it is necessary to consider the feasibility of structural adjustments in the actual modules during the preliminary optimization process, significant modifications may not be feasible. However, this section ignored these limitations and made substantial structural adjustments to the optimized design, aiming to achieve the extreme cooling performance of the rear-inlet module channel.

Upon analyzing the velocity field after preliminary optimization, it was evident that the layout of the air inlet on the rear wall of the module was no longer suitable for the current airflow path and needed to be replanned. The specific adjustments are shown in Fig. 17, marked as optimization I-4. The air inlet at the bottom of the heat exchange fin

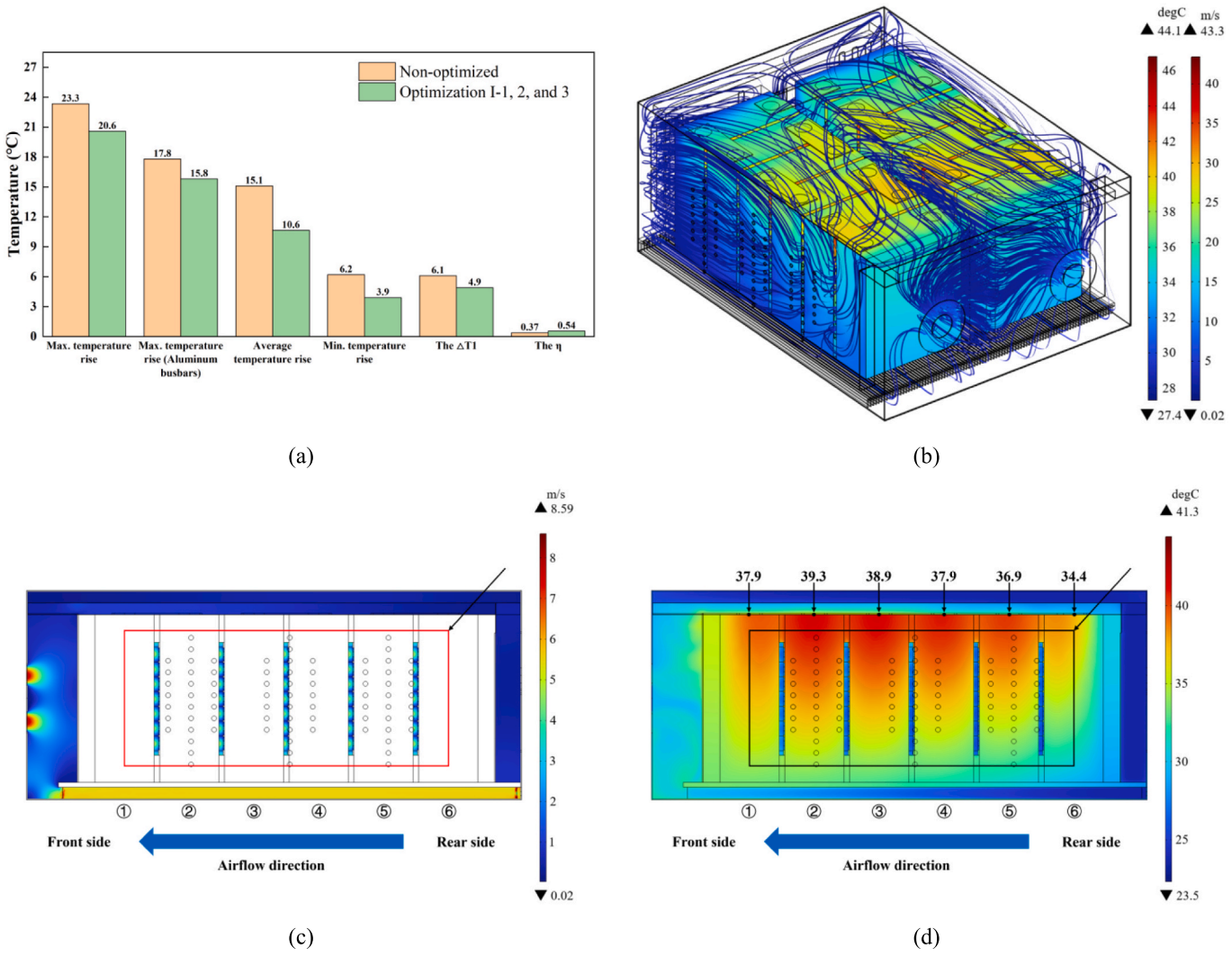


Fig. 14. Preliminary optimization results.

plate remained unchanged, while the upper part of the air inlet had been modified to include two vertical inlets on each side and a horizontal air inlet at the top. The vertical inlets on both sides facilitated the input of cooling air into the longitudinal main channels on both sides, and an additional horizontal inlet was introduced at the top to directly supply cooling air to the front row of harmonica pipes, thereby organizing the airflow inside the channel and reducing air turbulence. The side wall air inlet had the minimum airflow rate. In order to convert the module's air intake method to a pure rear-inlet system, the sidewall air inlets were eliminated. Finally, the adjustments made to optimizations I-1, 2, 3, 4, as well as the removal of the sidewall air inlets, were collectively referred to as optimization I for future optimization studies.

A novel structure of harmonica pipes was proposed in this paper, as shown in Fig. 18(a), which was divided into three sections: upper, middle, and lower. The upper and lower structures maintained sufficient heat exchange areas, while the transverse support ribs in the upper and lower sections provided enhanced structural support. Currently, the heat exchange principle of most harmonica pipes involves conducting heat from the cells to the harmonica pipes, and then transferring the heat to the cooling air. However, due to the presence of contact thermal resistance, the heat exchange efficiency is significantly reduced. Theoretically, the optimal heat exchange method is to eliminate the harmonica pipes and allow direct contact between the cell surfaces and the cooling air, which will result in optimal cooling performance. Nevertheless, the practical situations require the addition of harmonica pipes. Therefore, this paper introduced the new structure of harmonica pipes, which differed from traditional designs by relocating the vertical support structure in the middle to the vertical centerline. This modification almost doubled the contact area between the cooling air and the harmonica pipes, and additionally increased the area of direct contact between the cooling air and the surface of the cells. The advantages of this novel harmonica pipe structure included: while ensuring support for the cells, it not only increased the contact area with the cooling air, but also enhanced the direct contact area with the cell surfaces, thereby maximizing the heat exchange performance. Furthermore, the effects of the number of transverse supporting ribs m in the upper and lower sections and the width w of the harmonica pipes on the cooling performance were also investigated.

In addition, this paper optimized the design of the bottom heat exchange fin plate structure. Fig. 18(b) shows various heat exchange fin structures, where optimization III-1 represented the original unmodified structure. In optimization III-2, the fin orientation changed from longitudinal to transverse, and the red frames indicated the fin positions. Fins were placed at the bottom of each cell. Based on optimization III-2, optimization III-3 further moved the fin positions forward, removing the fins below the last row of cells while maintaining them under the first five rows. Although the original heat exchange fin plate could reduce the overall temperature rise, it did not meet the temperature difference

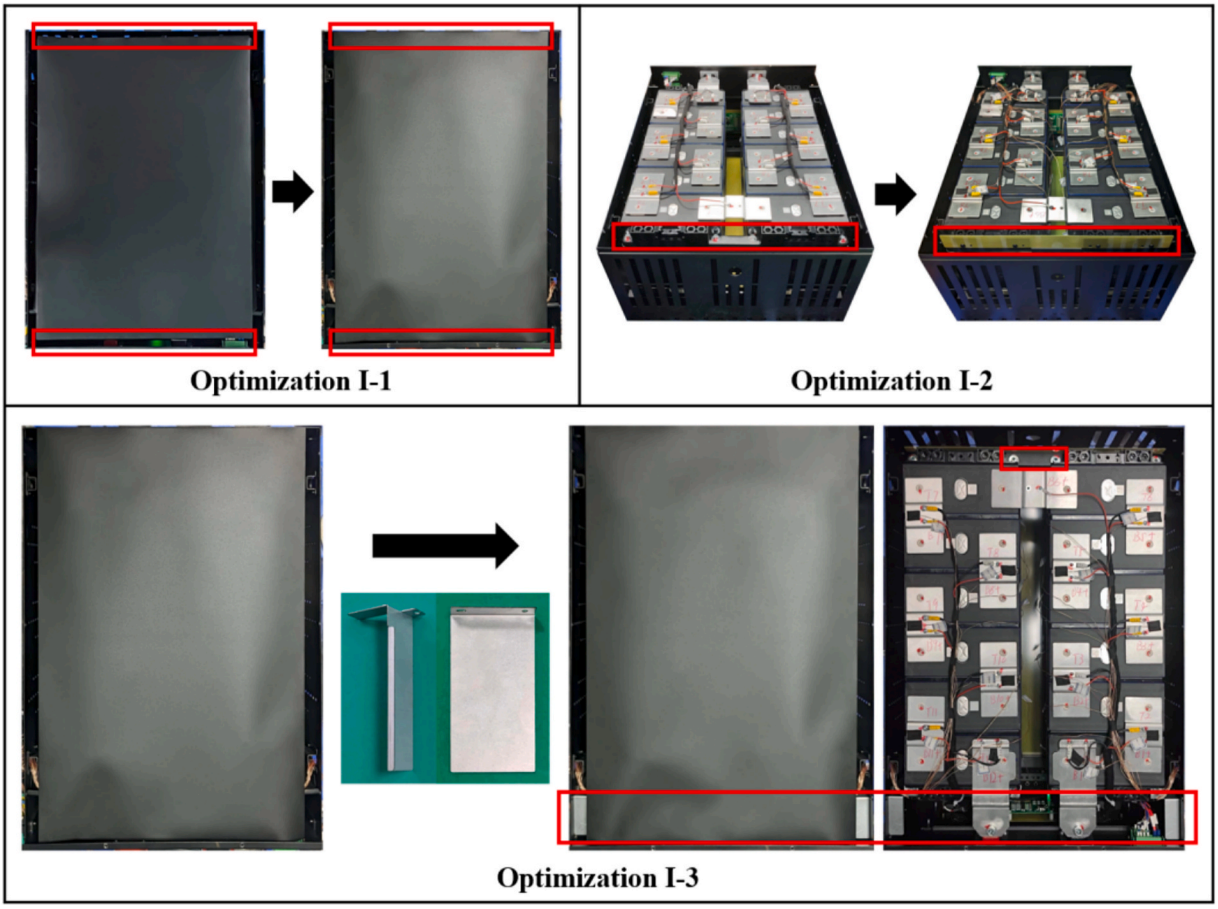
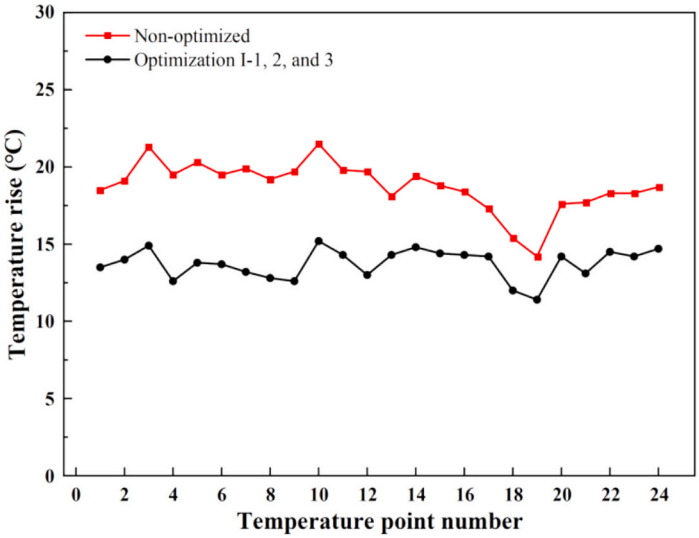


Fig. 15. Structural improvements in the experimental module.



	Temperature rise (°C)	Non-optimized	Optimization I-1, 2, and 3	ΔT	Percent
Aluminum busbars	Max.	21.5	15.2	6.3	29.3%
	Average	19.8	13.6	6.2	31.3%
	Min.	18.5	12.6	5.9	31.9%
	Difference	3.0	2.6	0.4	13.3%
Battery sidewalls	Max.	19.4	14.8	4.6	23.7%
	Average	17.7	13.8	3.9	22.0%
	Min.	14.2	11.4	2.8	19.7%
	Difference	5.2	3.4	1.8	34.6%

Fig. 16. Comparison of experimental temperatures before and after optimizations I-1, 2, and 3.

requirements. Therefore, changing the direction of the fins to transverse aimed to eliminate the adverse effects of longitudinal temperature differences within the heat exchange fins on the overall cell temperature difference. Due to the significant temperature difference between the last row of cells and the first five rows, optimization III-3 excluded the fins at the bottom of the last row. This adjustment aimed to increase the temperature of the last row of cells while enhancing the air velocity within the remaining fins to lower the temperature of the first five rows, ultimately reducing the overall temperature difference.

To investigate the effects of the rectification structure (optimization I), harmonica pipe structure (optimization II), and heat exchange fin plate structure (optimization III) on the temperature characteristics of the module, different optimization structures were combined together, as shown in Table 3. In group ⓪, the heat exchange fin plate was

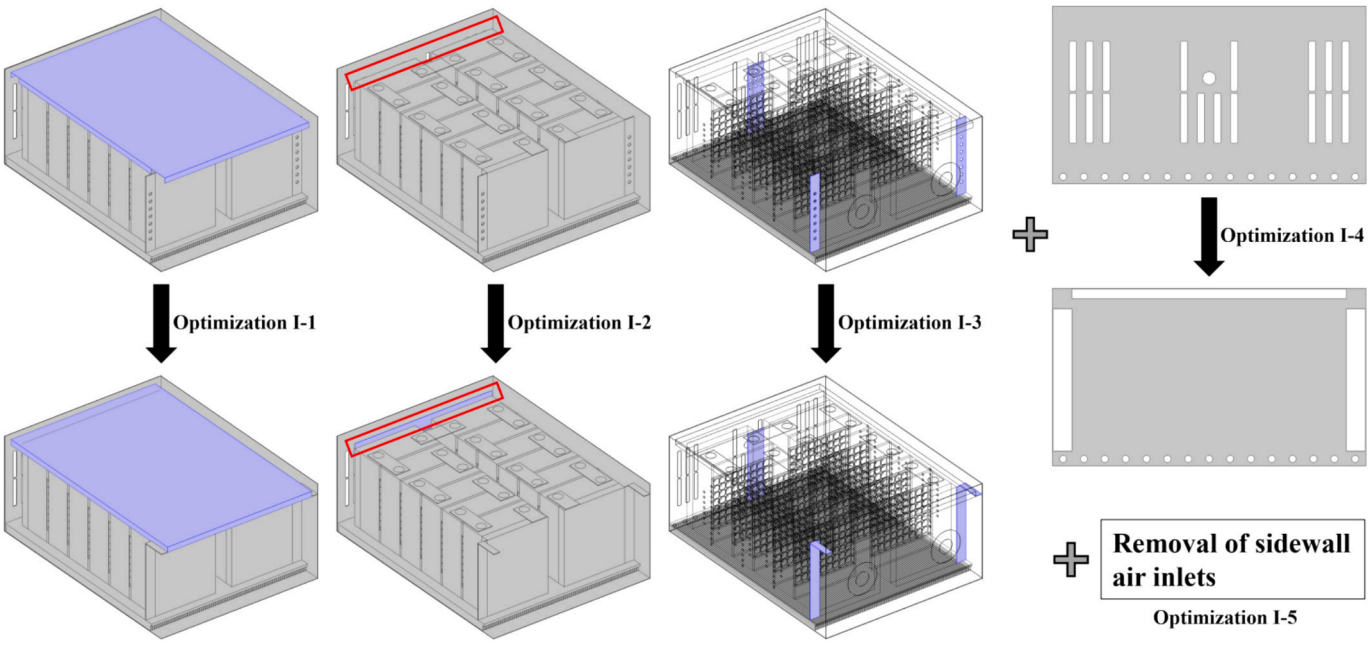


Fig. 17. All modified structures for optimization I.

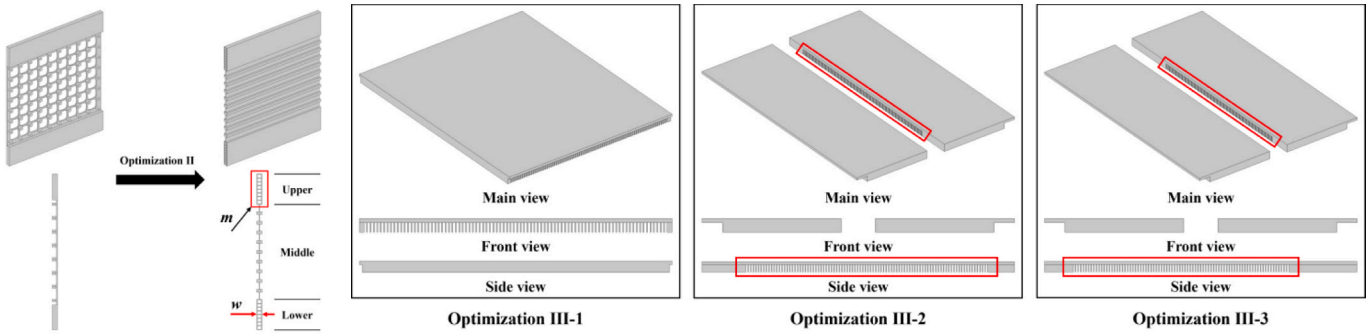


Fig. 18. All modified structures for optimization II and optimization III-1, 2, 3.

Table 3
Combinations of different modified structures.

		Optimization I	Optimization II	Optimization III-1	Optimization III-2	Optimization III-3
Only one optimization	Group ⓪					
	Group ①	√				
	Group ②		√			
	Group ③			√		
	Group ④				√	
	Group ⑤					√
Only two optimizations	Group ⑥	√		√		
	Group ⑦	√			√	
	Group ⑧	√				√
	Group ⑨		√	√		
	Group ⑩		√		√	
	Group ⑪		√			√
	Group ⑫	√	√			
All three optimizations	Group ⑬	√	√	√		
	Group ⑭	√	√		√	
	Group ⑮	√	√			√

removed from the bottom of the module, while the other structures remained unmodified.

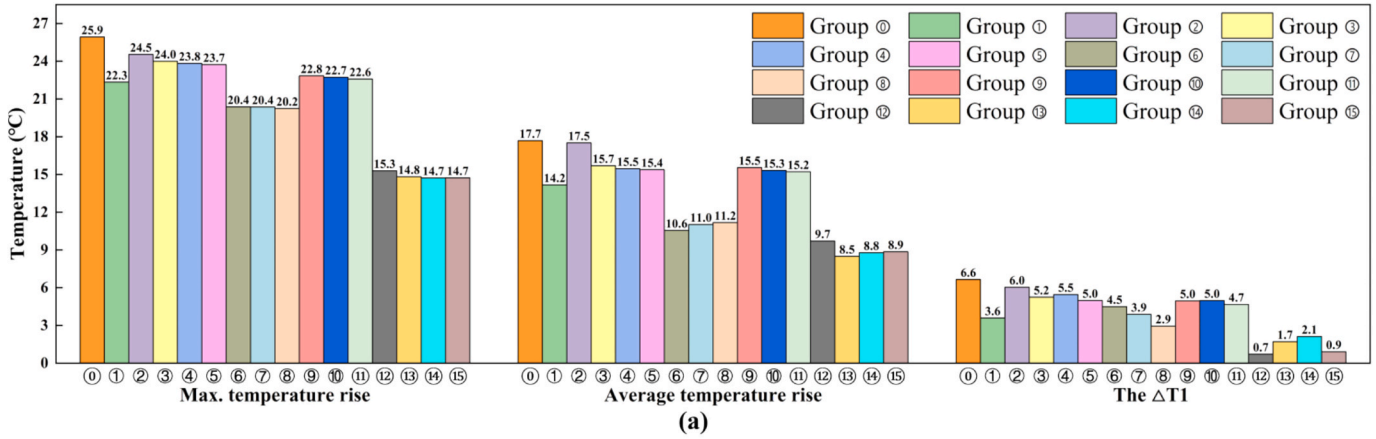
Fig. 19(a) compares the effects of different optimization groups, where the average temperature rise indicated the overall heat exchange efficiency of the flow channels, and the ΔT_1 represented the temperature distribution level. The average temperature rise of group ⑬ was the lowest, but the temperature difference was relatively large. Group ⑮ maintained a low average temperature rise and temperature difference, while achieving the minimum maximum temperature. Although the temperature difference of group ⑫ was the smallest, its average temperature rise was 0.8 ℃ higher than that of group ⑮, approaching 1 °C. Therefore, group ⑮ was ultimately selected for further optimization research.

Fig. 19(b), (c) and (d) show the effects of different groups, specifically indicating the differences in average temperature rise and the ΔT_1 between the former and latter groups. Fig. 19(b) presents the comparison between group ⓪ and group ①, group ② and group ⑫, groups ③④⑤ and groups ⑥⑦⑧, as well as groups ⑨⑩⑪ and groups ⑬⑭⑮. The purpose of this comparison was to explore the impact of optimization I, involving the rectification structures on cooling performance. It could be observed that the average temperature rise had been significantly improved in all cases. In terms of the ΔT_1, most comparisons also showed notable enhancement. This indicated that in any case, optimization I, which guided the cooling air to flow through the harmonica pipes and heat exchange fin plate, could effectively enhance the cooling performance of the module.

Fig. 19(c) compares group ⓪ with group ②, group ① with group ⑫, groups ③④⑤ with groups ⑨⑩⑪, as well as groups ⑥⑦⑧ with groups ⑬⑭⑮. This analysis aimed to explore the influence of the harmonica pipe structure, as characterized by optimization II, on cooling performance. It could be seen that among all the comparisons, whether it was the average temperature rise or the ΔT_1, the improvement observed between group ① and group ⑫ was the most significant, while the comparison results between groups ⑥⑦⑧ and groups ⑬⑭⑮ were intermediate. The improvements seen in the comparisons of group ⓪ with group ②, and groups ③④⑤ with groups ⑨⑩⑪ were very small and almost negligible. This indicated that only by combining optimization I and enhancing the harmonica pipe structure could the cooling performance be significantly improved. Analysis showed that under the conditions of established optimization I, the cooling air completely flowed through the harmonica pipes and the heat exchange fin plate, and the airflow velocity inside the harmonica pipes was relatively high. In this context, modifying the harmonica pipe structure effectively enhanced its inherent heat exchange performance. On the contrary, without optimization I, the impact of structural modifications could be ignored when the airflow velocity inside the harmonica pipes was low, indicating that the intrinsic heat exchange capability of the new harmonica pipes had not been effectively activated.

Fig. 19(d) compares the effects of group ⓪ and groups ③④⑤; group ① and groups ⑥⑦⑧; group ② and groups ⑨⑩⑪; and group ⑫ and groups ⑬⑭⑮. The analysis aimed to explore the influence of the heat exchange fin plate structure on cooling performance. According to the observations, with respect to average temperature rise, the heat exchange fin plates consistently demonstrated improvement in all cases. Notably, in the case of only optimization I, represented by the comparison of group ① with groups ⑥⑦⑧, the improvement remained the most significant. This indicated that the inherent heat exchange capability of the fin plates was fully activated when the airflow velocity within them was high. Conversely, when the airflow velocity was low, only a portion of their heat exchange capacity was utilized. Regarding the ΔT_1, when combined with Fig. 19(a), the comparison of different schemes: optimization III-1, optimization III-2, and optimization III-3, showed that the improvement effects of the heat exchange fin plates on the ΔT_1 were inconsistent. While some configurations improved temperature distribution, others may have worsened it. Optimization III-3 consistently achieved the best results in reducing the ΔT_1 compared with optimizations III-1 and III-2. This demonstrated that the novel heat exchange fin plate proposed in this study (optimization III-3) was capable of lowering the ΔT_1 under specific conditions.

Overall, the inherent heat exchange effects of the harmonica pipes



(a)

Group	ΔT	
	Average temperature rise (℃)	The ΔT_1 (℃)
⓪ vs. ①	3.5	3
② vs. ⑫	7.8	5.3
③④⑤ vs. ⑥⑦⑧	5.1/4.5/4.2	0.7/1.6/2.1
⑨⑩⑪ vs. ⑬⑭⑮	7/6.5/6.3	3.3/2.9/3.8

(b)

Group	ΔT	
	Average temperature rise (℃)	The ΔT_1 (℃)
⓪ vs. ②	0.2	0.6
① vs. ⑫	4.5	2.9
③④⑤ vs. ⑨⑩⑪	0.2/0.2/0.2	0.2/0.5/0.3
⑥⑦⑧ vs. ⑬⑭⑮	2.1/2.2/2.3	2.8/1.8/2

(c)

Group	ΔT	
	Average temperature rise (℃)	The ΔT_1 (℃)
⓪ vs. ③④⑤	2/2.2/2.3	1.4/1.1/1.6
① vs. ⑥⑦⑧	3.6/3.2/3	-0.9/-0.3/0.7
② vs. ⑨⑩⑪	2/2.2/2.3	1/1/1.3
⑫ vs. ⑬⑭⑮	1.2/0.9/0.8	-1/-1.4/-0.2

(d)

Fig. 19. Comparative results of different groups.

and the heat exchange fin plate could be effectively realized only when the cooling air inside the module flowed entirely through the harmonica pipes and the heat exchange fin plate, ensuring a high airflow velocity inside them. Under the condition of fully activating their intrinsic heat exchange effects, the novel harmonica pipe proposed in this study significantly improved both temperature rise and temperature difference. Although the novel heat exchange fin plate also contributed to reducing temperature rise and could lower temperature difference under specific conditions, its improvement effects were not as significant as those of the novel harmonica pipe.

Fig. 20 compares the effects of different numbers of ribs on the harmonica pipes. It was observed that as the number of ribs m increased, the maximum temperature rise and average temperature rise, as well as the ΔT_1 and the ΔT_2, first decreased and then increased. This indicated that there was an optimal number of ribs at $m = 5$, at which point both temperature rise and temperature difference reached their optimal states. To understand the reason for this optimal number of ribs, an analysis was conducted comparing the temperature and velocity distributions under different rib counts, as shown in Fig. 21. The black frames indicated the temperature and velocity distributions of the cooling air at the rib locations in the harmonica pipes. As the number of ribs increased, the temperature of the cooling air at the ribs rose, while the corresponding airflow velocity decreased. When $m = 0$, the cooling air temperature was the lowest and the airflow velocity was the highest. However, the heat exchange area was very small, and increasing the number of ribs enhanced the heat exchange area. When the number of ribs m increased to 11, the heat exchange area was significantly enhanced, but the flow area decreased and the flow resistance increased, resulting in a decrease in airflow velocity and, consequently, an increase in the temperature of the cooling air. Thus, the heat exchange efficiency was not optimal at this point. The optimum heat exchange effect occurred when both the heat exchange area and the corresponding airflow velocity were maximized. However, these two aspects could not be maximized simultaneously. Increasing the number of ribs improved the heat exchange area, but it reduced the airflow velocity. Therefore, there existed a balance point where the cooling air temperature at the ribs was kept relatively low (indicating a high airflow velocity) and the heat exchange area was also maximized. It was found that at $m = 5$, the cooling air temperature at the ribs remained at a lower level while the heat exchange area was moderate. Further increasing the number of ribs resulted in a noticeable rise in temperature and a significant decrease in airflow velocity. Thus, $m = 5$ represented the balance point between the heat exchange area and the airflow velocity, leading to the optimal overall cooling effect.

Fig. 22 illustrates the comparative effects of different widths w of harmonica pipes. It was observed that with the increase of width w, the maximum temperature rise and the average temperature rise, as well as the ΔT_1 and the ΔT_2, exhibited a trend of first decreasing and then increasing. This trend was closely related to the influence of the number of ribs, indicating the existence of an optimal value, specifically at $w =$ 10 mm. In Fig. 23, the temperature and velocity distributions for different widths w of harmonica pipes were compared, and the balance between heat exchange area and airflow velocity was also evident. When $w = 4$ mm, the heat exchange area was minimized and the corresponding airflow velocity was maximized. On the contrary, when $w =$ 13 mm, the heat exchange area reached its maximum value, but the airflow velocity was minimal. It could be inferred that the balance point occurred at $w = 10$ mm, at which point both the temperature rise and the temperature difference remained relatively low.

Thus, the optimal number of ribs m for the novel proposed harmonica pipes was determined to be 5, and the harmonica pipe width w was set to 10 mm, achieving the best overall heat exchange performance.

The performance comparison of the final structure is shown in Fig. 24(a), where the number of transverse ribs m in the upper and lower parts of the harmonica pipes in optimization II was 5, and the width w of the harmonica pipes was 10 mm. Compared with the original module, the maximum temperature rise of the surface of the cells in the optimized module decreased by 8.6 °C (36.9 %), the maximum temperature rise at the measurement points of the aluminum busbars decreased by 4.8 °C (28.2 %), and the average temperature rise of the surface of the cells decreased by 6 °C (39.7 %). The ΔT_1 decreased by 5.4 °C (88.5 %), while the ΔT_2 reduced by 1.3 °C (56.5 %). The η increased to 0.61 (64.9 %). The maximum temperature rise was less than 15 °C, and the recorded highest temperature was 38.2 °C, which was lower than 40 °C, thereby achieving a recognized safe temperature range. In addition, both values of the ΔT_1 and the ΔT_2 were $\leq$1 °C, indicating a good temperature distribution. Under conditions of 280 Ah at a 1C rate, while maintaining constant fan parameters and ensuring the overall module volume remained unchanged, the current temperature levels achieved were commendable. Furthermore, the final optimization of the rear-inlet module's flow channel structure had nearly achieved extreme cooling efficiency and performance.

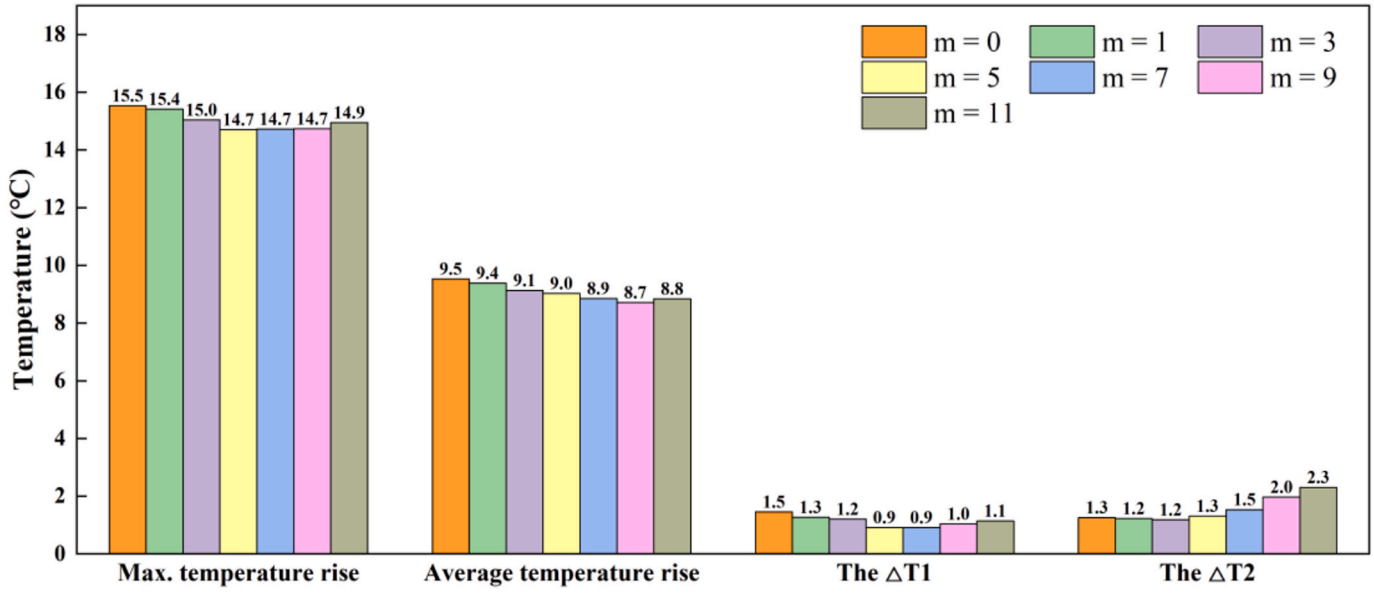


Fig. 20. Comparison of cooling performance under different m.

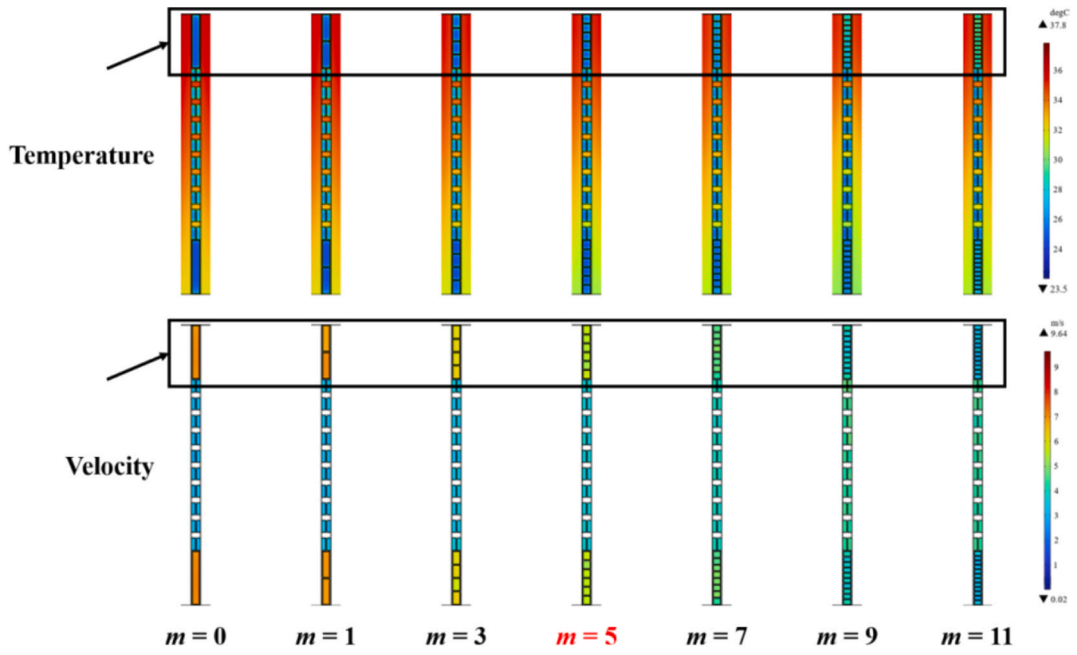


Fig. 21. Comparison of temperature and velocity distributions under different *m*.

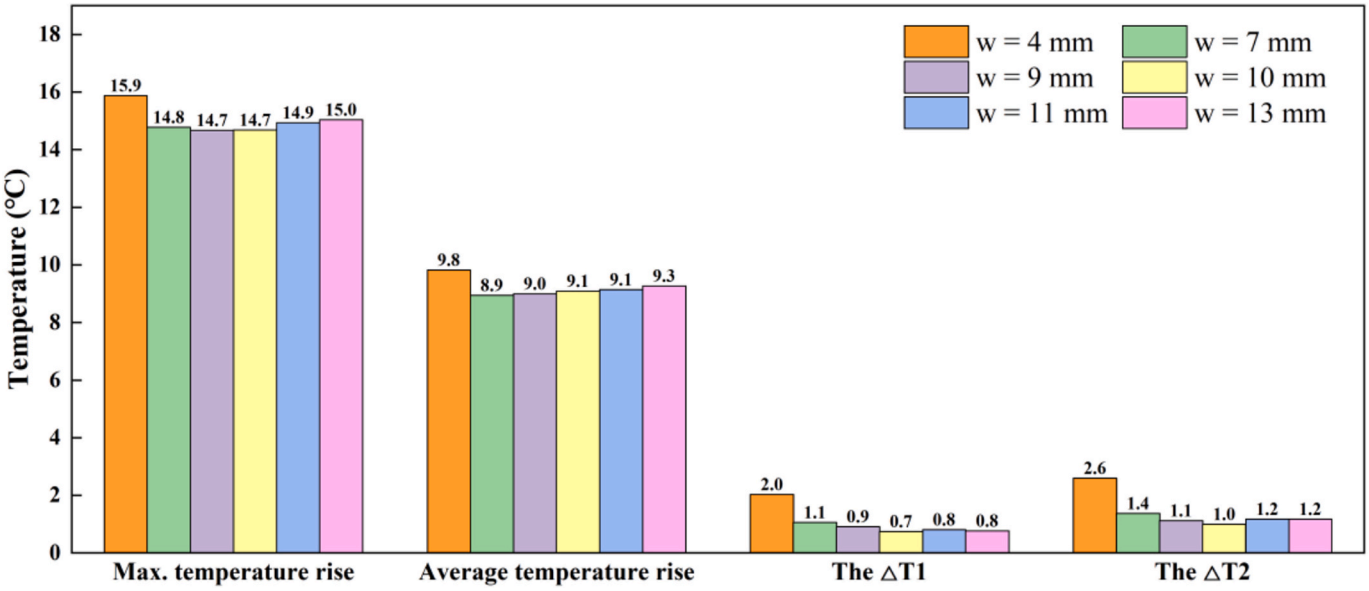


Fig. 22. Comparison of cooling performance under different *w*.

In this study, the experimental results for the air-cooling system showed that the temperature difference of the module after preliminary optimization was 2.6 °C. According to current Chinese National Standards for lithium-ion batteries in electrical energy storage, the maximum allowable temperature difference is 6 °C. Therefore, the temperature difference of the module after preliminary optimization was within acceptable limits. Additionally, simulation results indicated that the temperature difference of the module after final optimization did not exceed 1 °C. Thus, it is expected that the experimental temperature difference of the actual module after final optimization will be significantly reduced, although further research and validation are necessary.

As shown in Fig. 24(b), the flow trajectories of the cooling air within the entire module channel were orderly, and there were no flow conflicts in the flow field. All cooling air flowed along a predetermined path, specifically, all cooling air passed through the harmonica pipes and heat exchange fin plate. Fig. 24(c) and Fig. 24(d) illustrate that the inherent heat exchange capability of the novel harmonica pipes was favorable. Additionally, optimization I ensured that all cooling air flowed through the harmonica pipes and the heat exchange fin plate, effectively activating the excellent heat exchange capability of the novel harmonica pipes. This design effectively eliminated the heat generated by the cells, prevented the local heat accumulation, and ultimately lowered the temperature in the high-temperature regions of the cells. Moreover, the improved heat exchange fin plate not only eliminated the adverse effects of longitudinal temperature difference in the fins on the overall temperature difference of the cells, but also removed the fins below the last row of cells, successfully raising the temperature of the last row of cells. By lowering the temperature in the high-temperature areas and increasing the temperature in the low-temperature area, the overall

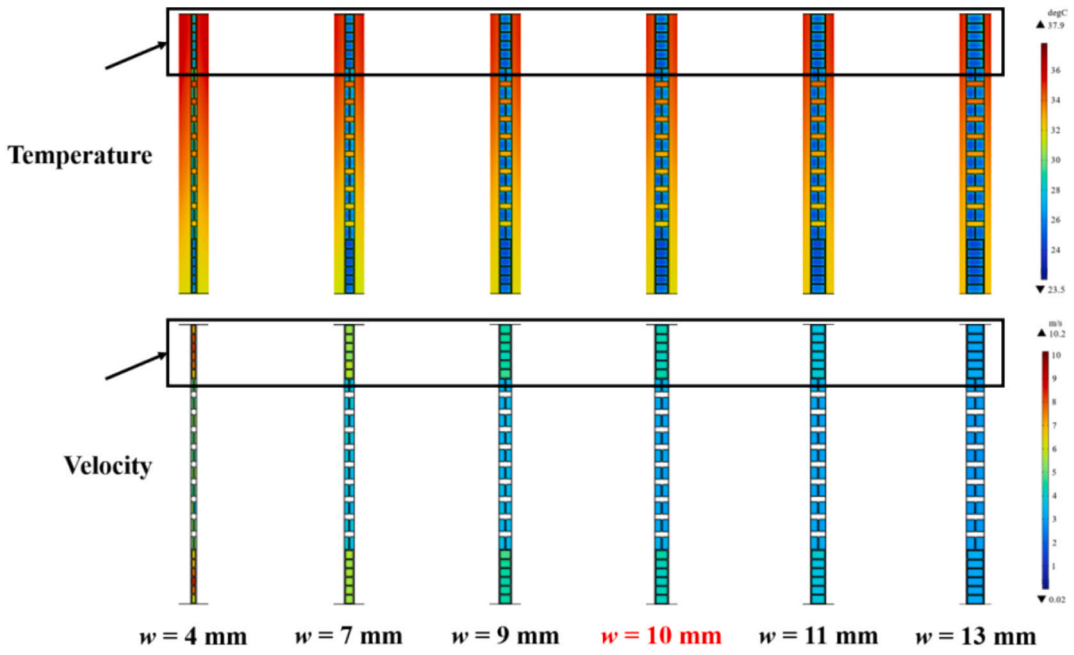


Fig. 23. Comparison of temperature and velocity distributions under different *w*.

temperature difference of the cells was significantly reduced. It could be concluded that under the premise of optimization I, both the structure of the novel harmonica pipes and heat exchange fin plate demonstrated excellent results in improving cooling efficiency and reducing temperature differences.

4.6. *Effects of ambient temperature and charging rate*

Under an ambient temperature of 23.5 °C and a charging rate of 1C, the final optimized structure demonstrated significant cooling improvement. Subsequent comparative analyses were conducted at varying ambient temperatures (20 °C, 23.5 °C and 30 °C) with a 1C charging rate to evaluate temperature characteristics. Since the maximum charging rate of the battery is 1C, corresponding to the highest heat generation rate, the temperature characteristics at a charging rate of 0.5C before and after optimization were also investigated.

The comparative results of different ambient temperatures and charging rates before and after optimization are presented in Fig. 25. It was observed that as the ambient temperature increased, the overall battery temperatures rose both before and after optimization, while the cooling rate decreased. However, the temperature differences decreased, leading to an improved temperature distribution within the module. Analysis indicated that the inlet air temperature for cooling was dependent on the ambient temperature. A decrease in inlet air temperature resulted in higher cooling intensity at the inlet, exacerbating the uneven distribution of cooling within the module. In contrast, an increase in inlet air temperature mitigated the uneven cooling distribution, thereby reducing temperature differences. Additionally, an increase in ambient temperature had a general heating effect on the module. Reducing the charging rate, and thus the heat generation rate, led to a decrease in both the overall battery temperatures and the temperature differences, while the cooling rate improved. This was attributed to the fact that, under constant external conditions, a lower heat generation rate naturally resulted in lower battery temperatures. Consequently, a larger proportion of the heat was removed by the cooling air, enhancing the cooling rate. Furthermore, due to the reduced overall heat generation of the battery, the temperature differences also decreased. In conclusion, the cooling performance of the optimized battery module was significantly improved under all operating conditions, demonstrating the universal applicability of the proposed novel optimized structure across various operating conditions.

5. Conclusions

This study innovatively proposed an airflow channel design with synergistic cooling enhancement for commonly used rear-inlet energy storage battery modules. A thermal management mathematical model for the battery module was developed, and an experimental platform was established. Experimental validation demonstrated good agreement with the model. Initially, constrained optimizations incorporating feasible module modifications were conducted through iterative simulations and experimental validation, achieving maximum performance improvements. Subsequently, comprehensive simulation-based optimizations were performed without practical constraints to investigate structural interactions and flow channel size effects. Finally, the influence of ambient temperature and charging rate was examined. The conclusions are as follows:

(1) Experimental findings:

During the entire experimental process, the highest temperature is recorded at the end of the second charging cycle. The temperature at the front side of the module is overall higher than that at the rear side, with the maximum temperature located near the second row of cells. Finally, based on the thermal imaging instrument's temperature distribution, it is inferred that the maximum temperature on the upper surface of cells is close to that of aluminum busbars at a certain moment, and it may even slightly exceed that of aluminum busbars. These new experimental findings can offer valuable guidance for the design optimization of charging and discharging strategies and thermal runaway warning in energy storage systems.

(2) Simulation results and proposed rectification structure:

Simulation results revealed that most of the cooling air flows out through longitudinal main flow channels without effectively contacting batteries, resulting in poor cooling efficiency. Therefore, a novel rectification structure is proposed, which involves adjusting the cover plate and windshields, along with adding a rear baffle at an appropriate

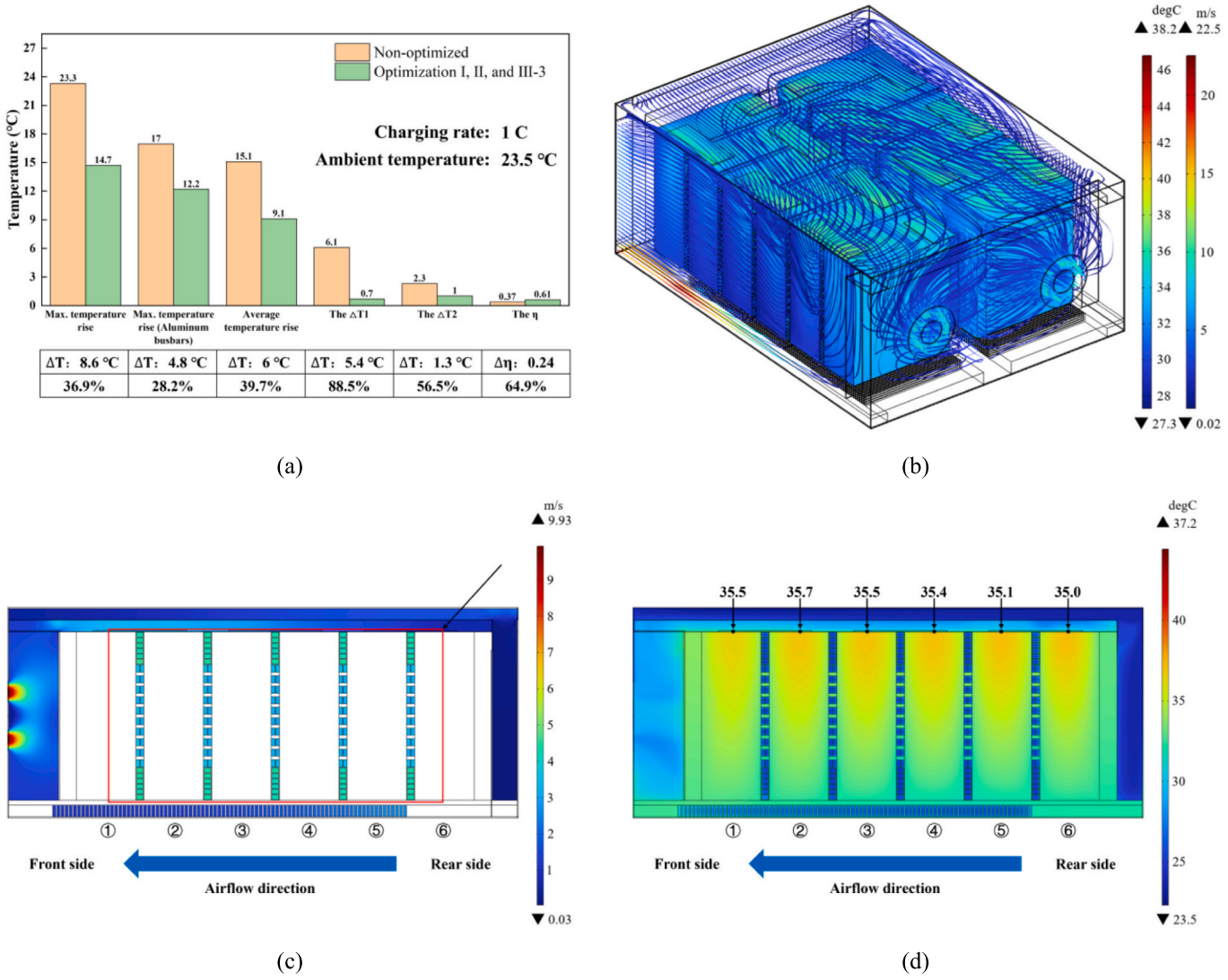


Fig. 24. The final optimized calculation results.

position. The tripartite structural enhancement improves convective heat transfer efficiency by maximizing air-battery interfacial contact while mitigating localized overcooling effects. After optimization, the cooling efficiency increases to 0.54 (45.9 %). Applying these preliminary optimizations to the actual module also yields considerable improvements, substantiating the effectiveness and practicality of simulation-based research in guiding the optimization of the module's flow channel structure.

(3) Comprehensive optimizations and synergistic effects:

Significant optimizations were conducted, including modifications to the novel rectification structure, the introduction of a novel harmonica pipe design, and a novel heat exchange fin plate structure. Simulation studies showed that the rectification structure consistently achieves the greatest improvement under all conditions. The harmonica pipe and heat exchange fin plate structures demonstrate superior heat exchange capabilities only when combined with the rectification structure. For the heat exchange fin plate, reorienting the fins horizontally and repositioning them forward effectively reduces temperature differences. Additionally, an optimal balance (5 ribs and a width of 10 mm) between the heat exchange area of harmonica pipe and airflow velocity is achieved, maximizing the integrated cooling effect. After final optimization, the cooling efficiency increases by 0.61 (64.9 %), and the maximum temperature rise decreases by 8.6 °C (36.9 %). Both the ΔT_1 and the ΔT_2 are reduced to $\leq$1 °C, representing reductions of 5.4 °C (88.5 %) and 1.3 °C (56.5 %), respectively. The final optimization achieves near extreme cooling efficiency and performance. Moreover, the cooling performance of the final optimization is significantly improved under varying ambient temperatures and charging rates, demonstrating its universal applicability across various operating conditions. In contrast to conventional single-factor optimization approaches, this study highlights the enabling amplification effect of the rectification structure on auxiliary structures. The synergistic interactions between composite configurations achieve thermal enhancement transcending linear superposition (manifested as "1 + 1 > 2" cooling efficiency gains), challenging the conventional hypothesis of structural independence. These findings establish a novel theoretical framework for modular battery pack design based on synergistic multi-structure interplay.

Through experimental and simulation methods, the temperature characteristics of the battery module were obtained. Building on this, the mutual influences of the rectification structure, harmonica pipe, and heat exchange fin plate structure on cooling performance were studied. Finally, the effects of flow channel size, ambient temperature, and charging rate were investigated. Based on this, some future research

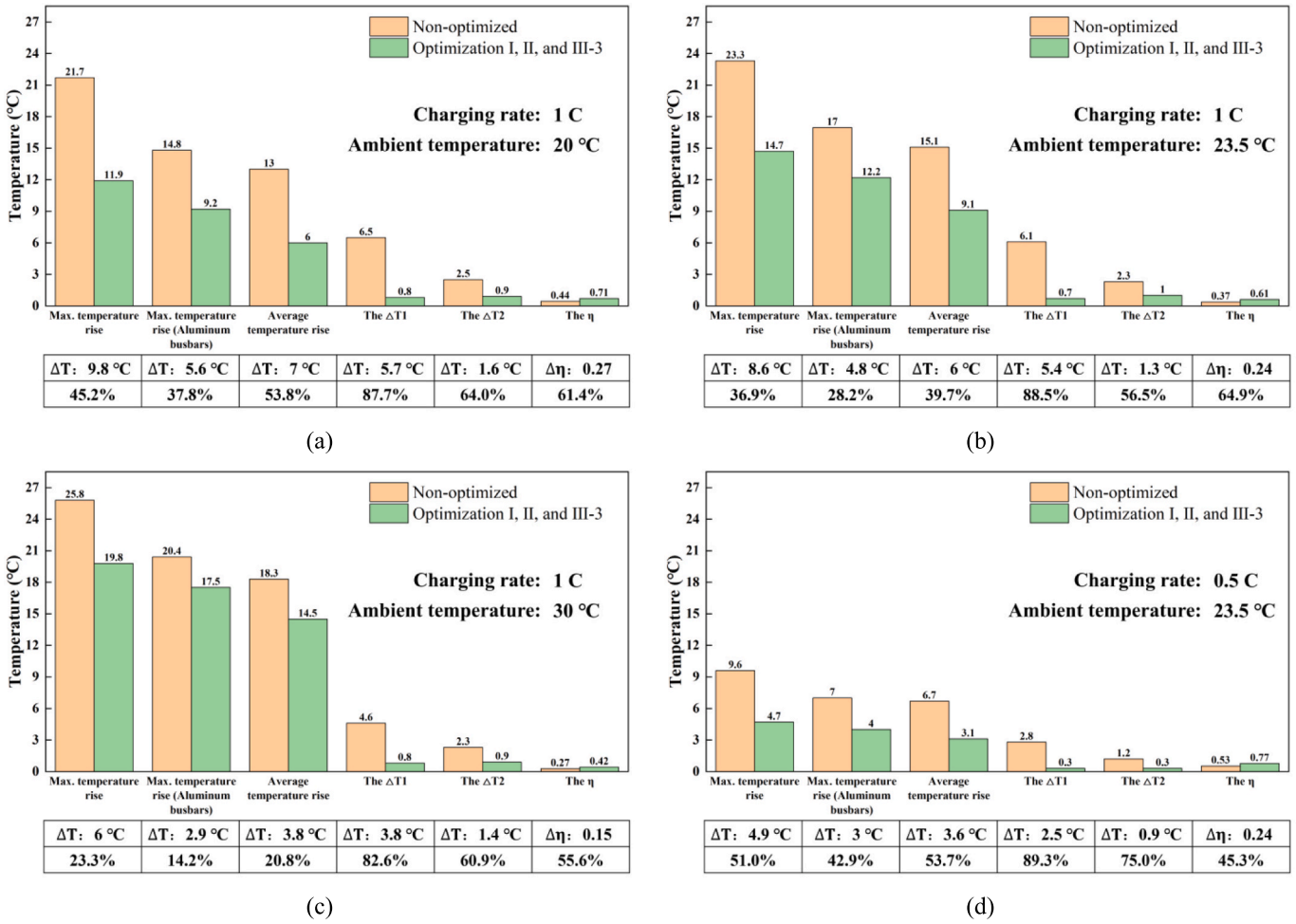


Fig. 25. Comparative results of different ambient temperatures and charging rates before and after optimization.

directions are proposed:

(1) Experimental validation of final optimized structure: Experimental studies on the application of the final optimized structure in actual modules should be conducted. Due to experimental constraints, only preliminary optimizations are applied to the actual module in this work. While simulation results for the final optimized structure are promising, its actual operational performance requires further validation.
(2) Innovative airflow channel design: Beyond the limitations of conventional module configurations, an innovative airflow channel structure can be proposed and investigated.
(3) Thermal management for other battery types: The current study focuses on prismatic batteries, and future research can explore thermal management systems for other types, such as cylindrical batteries.
(4) Long-term operational studies: The experiments in this study are limited to two charge–discharge cycles. Future work can investigate battery temperature and lifespan under long-term operational conditions. Moreover, these data can be combined with machine learning to predict battery temperature and lifespan.

Funding

This work was supported by the National Natural Science Foundation of China (52076007); Open Competition and Leading Project of China Huadian Cooperation Ltd. (JBGS2021-03).

Consent to participate

Not applicable.

Consent for publication

I have read and understood the publishing policy and submit this manuscript in accordance with this policy.

Ethics approval

Not applicable.

Declaration of competing interest

The authors declare that they have no known competing financial interests or personal relationships that could have appeared to influence the work reported in this paper.

Data availability

Data will be made available on request.

References

[1] Z. Zhu, T. Jiang, M. Ali, Y. Meng, Y. Jin, Y. Cui, W. Chen, Rechargeable batteries for grid scale energy storage, Chem. Rev. 122 (2022) 16610–16751, https://doi.org/10.1021/acs.chemrev.2c00289.

[2] X. Lin, Y. Jiang, H. Yu, M. Shi, B. Liu, X. Wen, Z. Zhou, A comprehensive investigation on the electrochemical and thermal inconsistencies for 280 Ah energy storage lithium-ion battery, Energy Convers. Manag. 315 (2024) 118750, https://doi.org/10.1016/j.enconman.2024.118750.
[3] Y. Zhang, W. Zhang, W. Kong, G. Wang, X. Tang, Comparative study on the performance of different thermal management for energy storage lithium battery, J. Energy Storage 85 (2024) 111028, https://doi.org/10.1016/j.est.2024.111028.
[4] J. E, F. Yi, W. Li, B. Zhang, H. Zuo, K. Wei, J. Chen, H. Zhu, H. Zhu, Y. Deng, Effect analysis on heat dissipation performance enhancement of a lithium-ion-battery pack with heat pipe for central and southern regions in China, Energy 226 (2021) 120336, https://doi.org/10.1016/j.energy.2021.120336.
[5] M. Nasiri, H. Hadim, Advances in battery thermal management: current landscape and future directions, Renew. Sustain. Energy Rev. 200 (2024) 114611, https://doi.org/10.1016/j.rser.2024.114611.
[6] Y. Zhang, W. Zhang, W. Kong, Numerical and experimental study on thermal behavior of prismatic lithium-ion battery for large-capacity energy storage, J. Energy Storage 83 (2024) 110620, https://doi.org/10.1016/j.est.2024.110620.
[7] P. Kumar, D. Chaudhary, P. Varshney, U. Varshney, S.M. Yahya, Y. Rafat, Critical review on battery thermal management and role of nanomaterial in heat transfer enhancement for electrical vehicle application, J. Energy Storage 32 (2020) 102003, https://doi.org/10.1016/j.est.2020.102003.
[8] T. Katrašnik, I. Mele, K. Zelič, Multi-scale modelling of Lithium-ion batteries: From transport phenomena to the outbreak of thermal runaway, Energy Convers. Manag. 236 (2021) 114036, https://doi.org/10.1016/j.enconman.2021.114036.
[9] X. Na, H. Kang, T. Wang, Y. Wang, Reverse layered air flow for Li-ion battery thermal management, Appl. Therm. Eng. 143 (2018) 257–262, https://doi.org/10.1016/j.applthermaleng.2018.07.080.
[10] Z. Lu, X. Yu, L. Wei, Y. Qiu, L. Zhang, X. Meng, L. Jin, Parametric study of forced air cooling strategy for lithium-ion battery pack with staggered arrangement, Appl. Therm. Eng. 136 (2018) 28–40, https://doi.org/10.1016/j.applthermaleng.2018.02.080.
[11] K. Chen, M. Song, W. Wei, S. Wang, Structure optimization of parallel air-cooled battery thermal management system with U-type flow for cooling efficiency improvement, Energy 145 (2018) 603–613, https://doi.org/10.1016/j.energy.2017.12.110.
[12] Y. Liu, J. Zhang, Design a J-type air-based battery thermal management system through surrogate-based optimization, Appl. Energy 252 (2019) 113426, https://doi.org/10.1016/j.apenergy.2019.113426.
[13] K. Chen, W. Wu, F. Yuan, L. Chen, S. Wang, Cooling efficiency improvement of air-cooled battery thermal management system through designing the flow pattern, Energy 167 (2019) 781–790, https://doi.org/10.1016/j.energy.2018.11.011.
[14] M. Wang, S. Teng, H. Xi, Y. Li, Cooling performance optimization of air-cooled battery thermal management system, Appl. Therm. Eng. 195 (2021) 117242, https://doi.org/10.1016/j.applthermaleng.2021.117242.
[15] C. Li, N. Cui, L. Chang, Z. Cui, H. Yuan, C. Zhang, Effect of parallel connection topology on air-cooled lithium-ion battery module: inconsistency analysis and comprehensive evaluation, Appl. Energy 313 (2022) 118758, https://doi.org/10.1016/j.apenergy.2022.118758.
[16] F. Zhang, M. Yi, P. Wang, C. Liu, Optimization design for improving thermal performance of T-type air-cooled lithium-ion battery pack, J. Energy Storage 44 (2021) 103464, https://doi.org/10.1016/j.est.2021.103464.
[17] Q. Yu, A. Abidi, M.Z. Mahmoud, E. Hasani Malekshah, H.Ş. Aybar, Numerical evaluation of the effect of air inlet and outlet cross-sections of a lithium-ion battery pack in an air-cooled thermal management system, J. Power Sources 549 (2022) 232067, https://doi.org/10.1016/j.jpowsour.2022.232067.
[18] H.A. Hasan, H. Togun, A.M. Abed, N. Biswas, H.I. Mohammed, Thermal performance assessment for an array of cylindrical Lithium-Ion battery cells using an Air-Cooling system, Appl. Energy 346 (2023) 121354, https://doi.org/10.1016/j.apenergy.2023.121354.
[19] L. Luo, Y. Liu, Z. Liao, J. Zhong, Optimal structure design and heat transfer characteristic analysis of X-type air-cooled battery thermal management system, J. Energy Storage 67 (2023) 107681, https://doi.org/10.1016/j.est.2023.107681.
[20] K. Chen, Z. Zhang, B. Wu, M. Song, X. Wu, An air-cooled system with a control strategy for efficient battery thermal management, Appl. Therm. Eng. 236 (2024) 121578, https://doi.org/10.1016/j.applthermaleng.2023.121578.
[21] Y. Suo, C. Tang, E. Han, Z. Chen, Comparative assessment and optimization among several plenum shapes and positions for the forced air-cooled battery thermal management system, J. Energy Storage 99 (2024) 113319, https://doi.org/10.1016/j.est.2024.113319.
[22] Kalkan, Thermal performance improvement of an air-cooled 18650 NMC battery module: a novel busbar design that acts as a turbulator, J. Energy Storage 88 (2024) 111613, https://doi.org/10.1016/j.est.2024.111613.
[23] J.H. Pu, R.C. Li, Y. Li, H. Zhang, M. Du, N. Hua, X. Zhang, The novel stereoscopic cooling plate designs and performance analysis for battery thermal management systems, Appl. Therm. Eng. 257 (2024) 124330, https://doi.org/10.1016/j.applthermaleng.2024.124330.
[24] W. Zuo, D. Li, Q. Li, Q. Cheng, Y. Huang, Effects of intermittent pulsating flow on the performance of multi-channel cold plate in electric vehicle lithium-ion battery pack, Energy 294 (2024) 130832, https://doi.org/10.1016/j.energy.2024.130832.
[25] Y. Wang, X. Xu, Z. Liu, J. Kong, Q. Zhai, H. Zakaria, Q. Wang, F. Zhou, H. Wei, Optimization of liquid cooling for prismatic battery with novel cold plate based on butterfly-shaped channel, J. Energy Storage 73 (2023) 109161, https://doi.org/10.1016/j.est.2023.109161.
[26] K. Monika, E.M. Punnoose, S.P. Datta, Multi-objective optimization of cooling plate with hexagonal channel design for thermal management of Li-ion battery module, Appl. Energy 368 (2024) 123423, https://doi.org/10.1016/j.apenergy.2024.123423.
[27] A. Kalkan, K. Celen, Bakirci, Multi-objective optimization of a mini channeled cold plate for using thermal management of a Li-Ion battery, Energy 251 (2022) 123949, https://doi.org/10.1016/j.energy.2022.123949.
[28] P.M. Sutheesh, J. Jose, T.K. Hotta, B. Rohinikumar, Numerical investigations on thermal performance of PCM-based lithium-ion battery thermal management system equipped with advanced honeycomb structures, Int. Commun. Heat Mass Transf. 158 (2024) 107937, https://doi.org/10.1016/j.icheatmasstransfer.2024.107937.
[29] X. Zhang, C. Liu, Z. Rao, Experimental investigation on thermal management performance of electric vehicle power battery using composite phase change material, J. Clean. Prod. 201 (2018) 916–924, https://doi.org/10.1016/j.jclepro.2018.08.076.
[30] J. Weng, Y. He, D. Ouyang, X. Yang, G. Zhang, J. Wang, Thermal performance of PCM and branch-structured fins for cylindrical power battery in a high-temperature environment, Energy Convers. Manag. 200 (2019) 112106, https://doi.org/10.1016/j.enconman.2019.112106.
[31] R.K. Sinha, A. Kumar, A. Maurya, A. Kumar, Thermal management of counter terminal lithium-ion battery using Bio-based PCM, Therm. Sci. Eng. Prog. 54 (2024) 102854, https://doi.org/10.1016/j.tsep.2024.102854.
[32] S. Abbas, Z. Ramadan, C.W. Park, Thermal performance analysis of compact-type simulative battery module with paraffin as phase-change material and flat plate heat pipe, Int. J. Heat Mass Transf. 173 (2021) 121269, https://doi.org/10.1016/j.ijheatmasstransfer.2021.121269.
[33] X. Chen, W. Yang, J. Shen, X. Xu, F. Zhou, Thermal performance of hybrid battery thermal management system with air cooling and phase change material embedding biomimetic variable section fins, Appl. Therm. Eng. 231 (2023) 120985, https://doi.org/10.1016/j.applthermaleng.2023.120985.
[34] S. Xin, C. Wang, H. Xi, Thermal management scheme and optimization of cylindrical lithium-ion battery pack based on air cooling and liquid cooling, Appl. Therm. Eng. 224 (2023) 120100, https://doi.org/10.1016/j.applthermaleng.2023.120100.
[35] R. Ren, Y. Zhao, Y. Diao, L. Liang, H. Jing, Active air cooling thermal management system based on U-shaped micro heat pipe array for lithium-ion battery, J. Power Sources 507 (2021) 230314, https://doi.org/10.1016/j.jpowsour.2021.230314.
[36] X. Yuan, A. Tang, C. Shan, Z. Liu, J. Li, Experimental investigation on thermal performance of a battery liquid cooling structure coupled with heat pipe, J. Energy Storage 32 (2020) 101984, https://doi.org/10.1016/j.est.2020.101984.
[37] S. Mousavi, A. Zadehkabir, M. Siavashi, X. Yang, An improved hybrid thermal management system for prismatic Li-ion batteries integrated with mini-channel and phase change materials, Appl. Energy 334 (2023) 120643, https://doi.org/10.1016/j.apenergy.2023.120643.
[38] H. Zhou, W. Li, W. Yang, X. Guo, L. Cui, T. Liu, A hybrid battery thermal management strategy that couples internal PCM with external air-jet cooling, J. Energy Storage 98 (2024) 113127, https://doi.org/10.1016/j.est.2024.113127.